AdRoit: an accurate and robust method to infer complex transcriptome composition

Tao Yang[1], Nicole Alessandri-Haber[1], Wen Fury[1], Michael Schaner[1], Robert Breese[1], Michael LaCroix-Fralish[2], Jinrang Kim[1], Christina Adler[1], Lynn E. Macdonald[1], Gurinder S. Atwal[1], Yu Bai[1, *]

Affiliations

1. Regeneron Pharmaceuticals, Inc., Tarrytown NY 10591
2. Cellular Longevity, Inc., San Francisco, CA 94103

*Corresponding author

Abstract

RNA sequencing technology promises an unprecedented opportunity in learning disease mechanisms and discovering new treatment targets. Recent spatial transcriptomics methods further enable the transcriptome profiling at spatially resolved spots in a tissue section. In controlled experiments, it is often of immense importance to know the cell composition in different samples. Understanding the cell type content in each tissue spot is also crucial to the spatial transcriptome data interpretation. Though single cell RNA-seq has the power to reveal cell type composition and expression heterogeneity in different cells, it remains costly and sometimes infeasible when live cells cannot be obtained or sufficiently dissociated. To computationally resolve the cell composition in RNA-seq data of mixed cells, we present AdRoit, an accurate and robust method to infer transcriptome composition. The method estimates the proportions of each cell type in the compound RNA-seq data using known single cell data of relevant cell types. It uniquely uses an adaptive learning approach to correct the bias gene-wise due to the difference in sequencing techniques. AdRoit also utilizes cell type specific genes while control their cross-sample variability. Our systematic benchmarking, spanning from simple to complex tissues, shows that AdRoit has superior sensitivity and specificity compared to other existing methods. Its performance holds for multiple single cell and compound RNA-seq platforms. In addition, AdRoit is computationally efficient and runs one to two orders of magnitude faster than some of the state-of-the-art methods.

Introduction

RNA sequencing is a powerful tool to address the transcriptomic perturbations in disease tissues and help understand the underlying mechanism to develop treatments[1]. Due to the presence of heterogeneous cell populations, bulk tissue transcriptome only characterizes the averaged expression of genes over a mixture of different types of cells. The identity of individual cell types and their prevalence remain unelucidated in the bulk data. However, knowledge of the cell type composition and gene expression perturbation at the cell type level is often critical to identifying disease-manifesting cells and designing targeted therapies. For instance, the constitution of stromal and immune cells sculpts the tumor microenvironment that is essential in cancer progression and control[2–6]. Excessive expression of cytokines in particular leukocyte types underlines the etiology of many chronic inflammatory diseases [7–11]. Such information cannot be directly read out from the bulk RNA-Seq.

Recent breakthroughs in spatial transcriptomics methods enable characterizing whole transcriptome-wise gene expressions at spatially resolved locations in a tissue section[12].

However, it remains challenging to reach a single cell resolution while measuring tens of thousands of genes transcriptome-wise. Some widely used technologies can achieve a resolution of 50-100 μm, equivalent to 3–30 cells depending on the tissue type[12,13]. The transcripts therein may originate from one or more cell types. Unlike the bulk RNA-seq, the profiling data at each spot contains substantial dropouts as merely a few cells are sequenced, imposing additional challenges to demystify the cell type content. We refer to bulk RNA-seq and spatial transcriptomics data at the multi-cell resolution as compound RNA-seq data hereafter.

The rapid development of single-cell RNA-seq (scRNA-seq) technologies has allowed for cell-type specific transcriptome profiling[14]. It provides the information missing from the compound RNA-seq data. Nevertheless, the technologies have low sensitivity and substantial noise due to the high dropout rate and the cell-to-cell variability. Consequently, scRNA-seq technologies require a large number of cells (thousands to tens of thousands) to ensure statistical significance in the results. In addition, the cells must remain viable during capture. These requirements render the scRNA-seq technologies costly, prohibiting their application in clinical studies that involve many subjects or cannot allow real time tissue dissociation and cell capture. Furthermore, scRNA-seq technologies may not be well suited to characterizing cell-type proportions in solid tissues because the dissociation and capture steps can be ineffective to certain cell types [15–17].

As sequencing at the single cell level is not always feasible, in silico approaches have been developed to infer cell type proportions from compound RNA-seq data[18–24]. The most common strategy is to conduct a statistical inference through the maximum likelihood estimation (MLE)[25] or the maximum a posterior estimation (MAP)[26] on a constrained linear regression framework, wherein the unobserved mixing proportion of a finite number of cell types are part of the latent variables to be optimized. [1921–24]The deconvolution methods are often applied to dissect the immune cell compositions in blood samples[27–31]. However, their performance in more complex tissues, such as the nervous, ocular, respiratory and gastrointestinal organs, remains unclear. These tissues often contain many cell types (10-10^2) and the difference among related cells can be subtle, rendering the deconvolution a challenging task. For example, a recent study on the mouse nervous system contains more than 200 cell clusters and many are highly similar neuronal subtypes[32].

Earlier works often utilized the transcriptome profiling of the purified cell populations to estimate the gene expressions per cell type (e.g. Cibersort)[19]. More recently, acquiring cell type specific expression from the scRNA-seq data was shown to be an intriguing alternative[21–24]. Though it provides higher throughput by measuring multiple cell types in one experiment, profiling at single cell level is substantially noisy. Deconvolution using scRNA-seq data as reference can be biased by noise non-relevant to cell identities if not treated properly. Moreover, the platform difference between the compound data and the single cell data cannot be ignored.

To overcome these challenges, additional information from the data may be considered. A recent method that weighs genes according to their expression variances across samples greatly improved the accuracy[22], highlighting the importance of gene variability in inferring cell type composition. Some other methods and applications have pointed out the importance of cell type specific genes[24,28,31,33]. In these works, the cell type specific expression was only used to select the input genes (e.g., markers). Nonetheless, it measures how informative a gene is in distinguishing cell types and thus can be incorporated as a part of the model. To address the platform difference between the compound data and the single cell data it is usually assumed there exists a single scaling factor or a linearly scaled bias for all genes that can be learned and corrected accordingly[22,23]. This assumption is hardly held because the impact of the platform difference to each gene is different. Though learning a uniform scaling factor would correct the difference in the majority of genes, a few genes that remain significantly biased can easily confound the estimation, especially under a linear model framework. Thus, a gene-wise correction should be considered.

In this work, we presented a new deconvolution method, AdRoit, a unified framework that jointly models the gene-wise technology bias, genes' cell type specificity and cross-sample variability. The method estimated the cell type constitution in the compound RNA-seq samples using relevant single cell data as a training source. Genes used for deconvolution were automatically selected from the single cell data based on their information richness. Uniquely, it uses an adaptively learning approach to estimate gene-wise scaling factors, addressing the issue that different platforms impact genes differently. The model of AdRoit is further regularized to avoid collinearity among closely related cell subtypes that are common in complex tissues. Over a comprehensive benchmarking data sets with a varying cell composition complexity, AdRoit showed superior sensitivity and specificity to other existing methods. Applications to real RNA-seq bulk data and spatial transcriptomics data revealed strong and expected biologically relevant information. We believe AdRoit offers an accurate and robust tool for cell type deconvolution and will promote the value of the bulk RNA-seq and the spatial transcriptomics profiling.

Results

Overview of the AdRoit framework

AdRoit estimates the proportions of cell types from compound transcriptome data including but not limited to bulk RNA-seq and spatial transcriptome. It directly models the raw reads without normalization, preserving the difference in total amounts of RNA transcript in different cell types. The method utilizes as reference the relevant pre-existing single cell RNA-seq data with cell identity annotation. It selects informative genes, estimates the mean and dispersion of the expression of selected genes per cell type, and constructs a weighted regularized linear model to infer percent combinations (Fig. 1a). Because sequencing platform bias impacts genes differently[15,34,35], a uniform scaling factor for all genes does not sufficiently eliminate such bias. A key innovation of AdRoit is that it uniquely adopts an adaptive learning approach, where the bias was first estimated for each gene, then adjusted such that more biased gene is corrected with a larger scaling factor (Fig. 1b).

We also attribute the success of AdRoit to the consideration of a comprehensive set of other relevant factors including genes' cross-sample variability, cell type specificity and collinearity of expression profiles among closely related cell types. The cross-sample variability of a gene confounds its biological expression variability due to the variety of cell types. The latter is referred as the cell type specific expression that helps identify the cell type. AdRoit weighs down genes with high cross-sample variability whilst weighs up those with an expression highly specific to certain cell types. The definition of cross-sample variability and cell type specificity also accounts for the overdispersion nature in counts data. Lastly, AdRoit adopted a linear model to ensure the interpretability of the coefficients. At the same time, AdRoit included a regularization term to minimize the impact of the statistical collinearity. Each of the factors contributes an indispensable part to AdRoit, leading to an accurate and robust deconvolution method for inferring complex cell compositions.

To evaluate the performance, we compared AdRoit with MuSiC[22] and NNLS[18,36] for bulk data deconvolution, and stereoscope[23] for spatial transcriptomics data deconvolution. When evaluating the algorithms, a common practice is to pool the single cell data to synthesize a "bulk" sample with the known ground truth of the cell composition. We measured the performance by comparing the estimated cell proportions with true proportions using four metrics: mean absolution difference (mAD), rooted mean squared deviation (RMSD) and two correlation statistics (i.e., Pearson and Spearman). Both correlations are included because Pearson reflects linearity, while Spearman avoids the artificial high scores driven by outliers when majority of estimates are tiny. Good estimations feature low mAD and RMSD along with high correlations. When estimating cell proportions for a synthetic sample, cells from this sample are excluded from the input single cell reference (i.e., leave-one-out) to avoid overfitting. We further applied AdRoit to real bulk RNA-seq data and validated the results by available RNA fluorescence *in-situ* hybridization (RNA-FISH) data. The estimates were further confirmed by relevant biology knowledge of human pancreatic islets. We also used AdRoit to map cell types on spatial spots, and the accuracy was verified by *in-situ* hybridization (ISH) images from Allen mouse brain atlas[37].

AdRoit excels in datasets with both simple and complex cell constitutions

We started with a simple human pancreatic islets dataset that contains 1492 cells and four distinct endocrine cell types (i.e., Alpha, Beta, Delta, and PP cells)[38] (Extended Data Fig. 1a; Supplementary Table 1). The synthesized bulk data were constructed by mixing the single cell data at known proportions. Though all three methods achieved satisfactory performance according to the evaluation metrics, AdRoit has slightly better performance as reflected by scatterplots of estimated proportion vs. true proportion (Extended Data Fig. 1b, Supplementary Table 2). It has moderately lower mAD (0.029 vs. 0.031 for MuSiC and 0.066 for NNLS), and RMSD (0.039 vs. 0.046 for MuSiC and 0.095 for NNLS) and comparable correlations (Pearson: 0.99 vs 0.98 for MuSiC and 0.93 for NNLS; Spearman: 0.97 vs 0.98 for MuSiC and 0.91 for NNLS) (Extended Data Fig. 1c). This performance was expected because there were only four cell types with very distinct transcriptome profiles. Deconvoluting such data was a relatively easy task for all three methods.

We then tested the methods on a couple of complex tissues that are more challenging to deconvolute. One is the human trabecular meshwork (TM) tissue. We acquired published single cell data that contains 8758 cells and 12 cell types from 8 donors[39]. The data include 3 similar types of endothelial cells, 2 types of Schwann cells and 2 types TM cells (Supplementary Fig. 1; Supplementary Table 3). Cells from each donor were pooled as a synthetic bulk sample. The cell type proportions vary from <1% to 43%. These proportions were the ground truth cell composition and were compared head-to-head with the estimated proportions inferred by AdRoit, MuSiC and NNLS. For each synthetic bulk sample, estimations were performed using a reference built from cells of other donors (i.e., leaving-one-out). In each of the 8 samples, the estimates made by AdRoit best approximated the true proportions. In particular, AdRoit had significantly lower mAD (0.016) and RMSD (0.025), and higher correlations (Pearson = 0.97; Spearman = 0.94), comparing to MuSiC (mAD = 0.038; RMSD = 0.06; Pearson = 0.83; Spearman = 0.73) and NNLS (mAD = 0.06; RMSD = 0.088; Pearson = 0.69; Spearman = 0.63) (Fig. 2a). We further assessed the deviation of the estimates from the true proportions for each cell type. AdRoit consistently had the lowest deviations from the true proportions for all cell types, as well as the lowest variation among 8 samples (Fig. 2b, blue dots), indicating a higher robustness over various cell types and samples. Notably, AdRoit only missed one rare cell type (true proportion = 0.3%) out of 12 cell types in one sample, while MuSiC missed 1 to 5 cell types in 6 of the 8 samples, and NNLS missed 3 to 7 cell types in all 8 samples (Supplementary Fig. 2, Supplementary Table 4).

AdRoit has better sensitivity and specificity

We next systematically addressed the sensitivity and specificity of these algorithms. In the context of the cell type deconvolution, a false negative occurs when the proportion of an existing cell type is predicted to be zero (or below a given threshold). Conversely, a non-zero prediction (or above a given threshold) of an absent cell type results in a false positive. False negatives and false positives measure the sensitivity and specificity of a deconvolution algorithm, respectively. Both quantities are crucial to establish the utility of the algorithm. Particularly, in real world applications, it is often difficult to know *a prior* what cell types exist in a bulk sample, users may inform the algorithm to consider more possible cell types than what are actually in the sample. False positive predictions in this situation would make the algorithm unusable.

We designed a simulation to test the sensitivity and specificity. we selected 6 out of the 12 cell types, i.e., Schwann-cell like cell, TM1, smooth muscle cell, melanocyte, macrophage and pericyte, from each donor sample and pooled them within that sample to synthesize 8 new bulk samples. The unselected 6 cell types are considered absent in the bulk samples. Some cell types in presence are highly similar to those in absence, challenging the programs to pinpoint the right cell type present in the bulk among similar candidates. We provided the full list of 12 single cell types as reference to the programs to estimate the cell type proportions. NNLS was excluded from this evaluation due to its low benchmarking performance observed earlier (Fig. 2a, b).

Consistently across 8 samples, AdRoit had very accurate estimates for the 6 present cell types, and zero or close-to-zero estimated values for the non-existing cell types in the synthetic bulk data. MuSiC was notably less accurate on the 6 selected cell types, meanwhile it had many non-negligible values (>1% for 26 out 48 estimates) of the 6 cell types excluded in the 8 synthetic samples (Fig. 2c, Supplementary Table 5). For example, smooth muscle cells accounted for ~14% in donor 4 but was largely missed (~0.03%) by MuSiC. We noted that TM2 had false non-zero estimates from both methods though not included. This is because TM2 is easily mistaken as TM1 due to their high similarity[39]. Nonetheless, AdRoit's estimates of TM2 were consistently small across samples (<1% for 44 out of 48 estimates), while MuSiC had significantly larger estimates of TM2 that occasionally even exceeded the TM1 estimates (donors 5 and 8 in Fig. 2c right). For a systematic comparison, we constructed the receiver operating characteristic (ROC) curve by varying the threshold of detection (i.e., a cutoff below which the cell type was deemed undetected) (Fig. 2d). AdRoit had significantly higher area under the curve (AUC) than MuSiC (0.95 vs. 0.74), implying a dominantly better sensitivity and specificity.

AdRoit outperforms in deconvoluting closely related subtypes

To further evaluate AdRoit when multiple cell subtypes present in a complex tissue, we performed scRNA-seq experiment on mouse lumbar dorsal root ganglion (DRG) from five mice. Following the standard analysis pipeline (Methods), we obtained 3352 single cells after quality control procedures. After clustering and annotation, we discovered 14 cell types including multiple subtypes of neuronal cells (Fig. 3a, Supplementary Table 6). The heatmap of the top marker genes showed distinct patterns of the major cell types as well as similar patterns of the subtypes (Extended Data Fig. 2a), and the cell type proportions varied from 0.5% to 33.71% (Extended Data Fig. 2b). These 14 cell types include 3 subtypes of neurofilament containing neurons (i.e., NF_Calb1, NF_Pvalb, NF_Ntrk2.Necab2), 3 subtypes of non-peptidergic neurons (i.e., NP_Nts, NP_Mrgpra3, NP_Mrgprd), and 5 subtypes of peptidergic neurons (i.e., PEP1_Dcn, PEP1_S100a11.Tagln2, PEP1_Slc7a3.Sstr2, PEP2_Htr3a.Sema5a, PEP3_Trpm8). Also discovered were tyrosine hydroxylase containing neurons (Th), satellite glia and endothelial cells. Such complex compositions formed a challenging testing ground for evaluating the ability to distinguish closely related cell types. We again did the leave-one-out deconvolution on five synthesized bulk samples.

AdRoit had highly accurate estimations on all cell types across samples (Fig. 3b). It is worth to mention that, for the rare cell types that account for less than 5%, AdRoit still had a good estimation that is fairly close to the true proportions and never missed a single cell type, showing that AdRoit is very robust on rare cell types. For example, 0.51% endothelial cells were predicted to be 0.35%, and 1.05% NF2_Ntrk2.Necab2 cells were predicted to be 0.85% (Supplementary Fig. 3, Supplementary Table 7). On the contrary, MuSiC and NNLS were notably less accurate, especially for the cell types less than 5%, and missed multiple cell types including some large cell clusters taking account of ~10% (PEP1_Slc7a3.Sstr2 cells of Sample5). We further examined how much the variability of the estimates was in each individual sample. We computed the 4 metrics to evaluate the performance on each of the 5 synthetic samples and compared them head-to-head among the algorithms. This fine comparison showed AdRoit significantly outperformed MuSiC and NNLS on every sample (Fig. 3c). Further, the performance metrics of AdRoit were highly consistent across samples with the lowest variability among the three methods.

AdRoit excels on simulated spatial transcriptomics data

Given the promising performance on complex tissues, we continued to test AdRoit's applicability to spatial transcriptomics data. Spatial transcriptomics data differs from bulk RNA-seq data in that each spot only contains transcripts from a handful of cells (3-30)[12]. Some of the spots contain multiple cells of the same type, while others may have mixtures of cell types at varying mixing percentages (e.g., spatial spots at the boundary of different cell types). Also, because the mixture is a pool of only a few cells, the variations across spatial spots are expected to be greater than in bulk samples. We simulated a large number of spatial spots (3200 in total) by using sampled cells from the DRG single cell data above (Methods), then compared AdRoit with Stereoscope over a range of simulation scenarios.

We first tested whether the methods could correctly infer a single cell type when the spots contain cells from that same type. For each of the 14 cell types from DRG, we sampled 10 cells and pooled them to form a spatial spot. We repeated the simulation for 100 times for a robust testing, then used the full set of 14 cell types as reference to deconvolute the 1400 simulated spots. Both methods were able to identify the correct cell types with indistinguishable accuracy on the simulated cell types (i.e., estimates close to 1) and comparably low estimated values (i.e., estimates close to zero) for other cell types not included when simulating the spots (Extended Data Fig. 3).

We then continued a difficult scenario where we sampled cells from the 5 PEP subtypes and mixed them. We created three simulation schemes for a comprehensive evaluation: 1) 5 PEP subtypes had same percent of 0.2; 2) PEP1_Dcn was 0.1 and the other 4 were 0.225; 3) PEP1_S100a11.Tagln2 and PEPE1_Dcn were 0.1, PEP2_Htr3a.Sema5a and PEP1_Slc7a3.Sstr2 were 0.2, and PEP3_Trpm8 was 0.4. Again, each simulation scheme was repeated 100 times. Under each scheme, the estimates by AdRoit consistently centered around true proportions and the other cell types had very low estimated values (close to zero) (Fig. 4a, Supplementary Table 8). In comparison, though the estimates for the other cell types were also generally close to zero, the estimates of the PEP cells by Stereoscope systematically deviated from the true proportions for all three simulated schemes except for PEP1_S100a11.Tagln2.

We further expanded the simulated spatial spots to the mixture of 3 NP cell types and mixture of 3 NF cell types. In addition, we sampled NP_Mrgpra3 cells and mixed them with other distinct cell types (i.e., Th, satellite glia and endothelial), as well as NF_Calb1 cells mixed with other distinct cell types, and PEP3_Trpm8 mixed with other distinct cell types. For all these simulated spatial spots, AdRoit's estimates were consistently centered at true proportions, whereas Stereoscope's estimates deviated in almost all simulated schemes (Extended Data Fig. 4, Supplementary Table 8). We speculate the main reason Stereoscope underperformed at these simulated spots is that it normalizes the total UMI counts to the same number for all cells. In real world, a spatial spot is unlikely to be a pool of cells that have the same total RNA transcripts sampled, especially when a spot contains different cell types (e.g., immune cells have about 10-fold less total UMIs than the neuronal cells or subtypes of neuronal cells). Our simulation pooled the sampled cells by adding up the raw UMI counts per gene, which we believe best mimics the real data.

Next, we asked how sensitive the methods are in detecting rare cell populations. We simulated mixtures of 3 PEP subtypes (i.e., PEP1_Slc7a3.Sstr2, PEP2_Htr3a.Sema5a, PEP3_Trpm8) with a series of low percent PEP3_Trpm8 (from 0.01 to 0.1 by 0.01), and the other two cell types sharing the rest percentage equally (Methods). At each given percent, the simulation was repeated 100 times. We then checked how accurately the percent of PEP3_Trpm8 cells was estimated. The medians of AdRoit's estimates were always close to the true proportions (Fig. 4b, red lines), whereas that of Stereoscope's estimates were largely lower than true proportions. Stereoscope also missed the majority of PEP3_Trpm8 cell type when the simulated proportion was below 0.06. This comparison implied AdRoit is more advantageous in detecting low percent cells. For a complete comparison, we also simulated 5 other types of cell mixtures in the same way. At each given low percent, we computed how many times out of 100 the low percent cell component was detected (estimates > 0.005). AdRoit had systematically higher detection rates, as well as higher consistency across different cell mixtures (Fig. 4c, Supplementary Table 9). Notably, at a simulated percent of 5%, AdRoit achieved >90% of detention rate, making it a powerful tool in detecting rare cells.

Though MuSiC was not designed for deconvoluting spatial spots, theoretically it also can be applied to spatial transcriptomics data. We thus also compared AdRoit to MuSiC on the same sets of simulation data above. We observed AdRoit was also significantly more accurate over all simulation scenarios of spatial spots (Fig. 4a, Extended Data Fig. 3 and 4, Supplementary Fig. 4), and more sensitive when detecting low percent cells (Fig. 4b, c, Supplementary Fig. 5).

Application to real bulk RNA-seq data of human pancreatic islets

Though using synthetic bulk data based on mixing of single cells is a useful benchmarking strategy, the bulk and single cell RNA-seq often use distinct RNA library preparation and sequencing protocols. The capability of a method to deconvolute real bulk samples shall be addressed to ensure it is useful in the real-world applications. We acquired 70 real human pancreatic islets bulk samples from published studies[38,40,41] (Supplementary Table 10) and used single cell data of the same tissue[38] as reference to infer the percentages of 4 endocrine cell types (i.e., Alpha, Beta, Delta, PP). The 70 bulk samples were collected from 39 distinct donors, including 26 healthy donors, and 13 donors with type 2 diabetes (T2D). Each donor contributed 1 to 5 replicated bulk RNA samples.

Replicates from the same donor are expected to have similar compositions and thus were used to assess the reproducibility of the estimates from AdRoit. For all cell types, AdRoit had highly consistent estimates for the same donors (Fig. 5a, Supplementary Table 11). The average standard deviations did not exceed 1% for all 4 cell types (i.e., Alpha: 0.010; Beta: 0.008; Delta: 0.004; PP: 0.002). To seek an independent validation, we obtained cell sorting results by RNA-FISH for 4 of the 39 donors[38] (Supplementary Table 12). The estimated cell proportions of the 4 were highly consistent with the percentages measured by RNA-FISH (Fig. 5b), and the consistency held for both major cells (Alpha and Beta) and the minor cells (Delta and PP). Reproducibility and independent validation showed AdRoit is reliable in deconvoluting real bulk RNA-seq data.

We then asked if AdRoit can detect known biological differences between healthy and T2D donors. Loss of functional insulin-producing Beta cells is a prominent characteristic of T2D[42–44], typically reflected by elevated level of hemoglobin A1c (HbA1c)[45,46]. Among the healthy donors, the majority of Beta cell proportions estimated by AdRoit ranged from 50% to 75% (Fig. 5c), agreed with the known percent range of Beta cells in human islets tissue[47,48]. A significant decreasing of the estimated Beta cell proportions was seen in T2D patients (P value = 4.1e-6). Further, a linear regression of estimated Beta cell proportions on HbA1c levels showed a statistically significant negative association (P value = 1.8e-6). AdRoit adequately reflected the cell composition difference between healthy donors and T2D patients.

Application to mouse brain spatial transcriptomics

We lastly demonstrated an application to the real spatial transcriptomics data. Given the molecular architecture of brain tissue has been well studied, we chose mouse brain spatial transcriptomics data generated by 10x genomics, containing 2703 spatial spots (Methods). The reference single cell data were acquired from an independent study which contains a comprehensive set of nervous cell types in brain[32]. We curated the cell types by merging highly similar clusters and came down to a consolidated set of 46 distinct brain cell types (Methods, Supplementary Table 13).

The cell contents inferred by AdRoit per spot appear to accurately match the expected cell types at that location (Extended Data Fig. 5, Supplementary Table 14). For example, the three subtypes of cortex excitatory neurons each occupied a sub-area in the cerebral cortex region. As another example, the shape of hippocampal region was delineated by the estimated percentages of dentate gyrus granule/excitatory neurons. For an independent validation, we checked the consistency between estimated cell types with the *in-situ* hybridization (ISH) images from Allen mouse brain atlas[49]. We chose 4 genes highly expressed in 4 brain regions respectively, i.e., Spink8 for hippocampal field CA1, C1ql2 for dentate gyrus, Clic6 for choroid plexus, and Synpo2 for thalamus[32]. The spots enriched with the 4 cell types (i.e., hippocampal CA1 excitatory neuron type 2, dentate gyrus granule neuron type 2, choroid plexus cell, thalamus excitatory neuron type 1), as mapped by AdRoit, precisely co-localized with the strong signals of the 4 marker genes on the ISH images respectively (Fig. 5d). This agreement confirmed that the spatial mapping of cell types by AdRoit is reliable.

Computational efficiency

Besides the accuracy and robustness, another major advantage of AdRoit is its magnitude higher computational efficiency. AdRoit uses a two-step procedure to do the inference. The first step prepares the reference on single cell data where per-gene means and dispersions are estimated, and cell type specificity is subsequently computed. The built reference can be saved and reused. We tested the running time on the reference building using the aforementioned mouse brain single cell dataset containing ~15,000 cells. It took about 4.5 minutes on a CPU that has 24 cores (23 used for parallel computing). The second step inputs the built reference and target compound data and does the estimation. Deconvoluting ~2700 compound RNA-seq samples took around 5 minutes. Therefore, AdRoit in total took less than 10 minutes and ~3Gb memory usage on a regular CPU. As a comparison, MuSiC took about 1 hour and 37 minutes on the same data using the same CPU. Stereoscope ran about 24 hours continuously with the published parameter setting (-scb 256 -sce 75000 -topn_genes 5000 -ste 75000 -lr 0.01 -stb 100 -scb 100) on a powerful V100 GPU with 80 cores and 16G memory, which is prohibitive for seeking a quick turnaround.

Discussion

In this work we have demonstrated that AdRoit is capable of deconvoluting the cell compositions from the compound RNA-seq data with a leading accuracy, measured by the consistency between the true and predicted cell proportions. Its advantage over the existing state-of-the-art methods was verified over a wide range of use cases. In particular, AdRoit excelled in complex tissues composed of more than ten different cell types with wide range of cell proportions (e.g., trabecular meshwork, dorsal root ganglion). In both cases, AdRoit performed significantly better than the comparators MuSiC and NNLS on deconvoluting bulk RNA-seq data. AdRoit is also more accurate and sensitive than Stereoscope in demystifying spatial transcriptomics spots, especially in detecting low percent cells. Previous benchmarking often assumed the types of cells in the synthetic bulk data are not more or less than the cell types collected in the reference, and thus the only unknown was the proportion of each cell type. This assumption may not hold. Missing existing cell types or false predictions of non-existing ones can hinder the utility of an algorithm. Thus, besides the overall accuracy, we also examined the sensitivity and specificity of the algorithms. We observed a superior sensitivity and specificity in AdRoit, an important leverage for its usage in practice.

The reference single cell data used by AdRoit came from different platforms, such as the 10x Genomics Chromium Instrument (the mouse dorsal root ganglion), and the Fluidigm C1 system (the human pancreatic islets data). AdRoit consistently exhibited excellent performance across all benchmarking datasets independent of their single cell sequencing technology platforms. More importantly, this statement holds not only for deconvoluting the synthesized bulk data, but also for the real bulk RNA-seq data. The latter typically does not apply the unique molecular barcoding and requires a significantly different cDNA amplification procedure from what is used in the single cell RNA-seq (Methods). Besides, the sequencing depth, read mapping and gene expression quantification are dissimilar as well. The fact that AdRoit accurately dissected the cell compositions in the real bulk samples based on the single cell reference data further supports its cross-platform applicability.

We attribute the power of AdRoit to its comprehensive modeling of relevant factors. Firstly, we think a common rescaling factor is not sufficient to correct the platform difference between single cells and the compound data. Rather, the impact of platform difference to genes is quite different and hardly is linearly scaled. Correcting such differences entails rescaling factors specifically tailored to each gene. AdRoit uses an adaptive learning approach to estimate such gene-wise correcting factor and does the correction in a unified model. In addition, the contribution of a gene in a cell type to the loss function is jointly weighted by its specificity and variability in a cell type, where specificity and variability are defined in a way accounting for the overdispersion property of counts data. Our observations over the multiple benchmarking dataset also show that the coexistence of similar cell types may have induced a collinearity condition that negatively impacted the regression-based methods developed by others. Being able to alleviate this problem gives AdRoit an edge to outperform. All these factors help AdRoit to distinguish similar cell clusters while sensitive enough to separate rare cell types.

Technically, the input profiles of individual cell types to AdRoit does not necessarily come from the single cell RNA-seq. Bulk RNA-seq profiles of individual isolated cell types can be used as well. Nevertheless, using single cell RNA-seq data as the reference has a few key advantages. It is a high throughput approach wherein multiple cell types can be interrogated simultaneously. Prior knowledge of the cell types in presence as well as their specific gene markers are not required, which allows novel cell types to be identified. Although detection of lowly expressing genes has been a challenge for the single cell RNA-seq, significant enhancements have been demonstrated. For example, the number of detectable genes currently can reach an order of 10,000 per cell and keeps improving[50]. As AdRoit focuses on the informative genes whose expressions are generally high, the detection limit of the single cell RNA-seq does not impose a significant drawback. Indeed, given the single cell reference profiles, AdRoit successfully deconvoluted the real bulk RNA-seq data and spatial transcriptomics data. The results suggest that, besides enriching our understanding of the bulk transcriptome data, AdRoit can leverage the usage of the vast amount and continuously growing single cell data as well.

AdRoit is a reference-based deconvolution algorithm. A comprehensive collection of the possible cell components is important. However, completeness may not always be guaranteed. Even with the single cell acquisition that is independent of prior knowledge, rare and/or fragile cell types may not survive through the capture procedure and hence are excluded. It is also difficult to generate a solid reference profile for cells that are versatile from sample to sample (e.g., tumor cells). Currently AdRoit deals implicitly with the components unknown to the reference. If an unknown cell type reassembles one of the referenced ones, it may be considered as part of the known cell type and their joint population is predicted. Such an outcome is acceptable as treating two similar cell types as one is still biologically meaningful although the resolution of the system may be compromised. If the unknown component is dissimilar to all the known ones, it will be ignored by AdRoit because its representative markers are unlikely among the top weighted genes associated with the known components. At the same time, the distinct component is expected to have a unique gene expression pattern and thus unlikely interferes significantly with the gene expressions from the known cell types. Therefore, AdRoit essentially deconvolutes the relative populations among the known cell components. For example, AdRoit was able to correctly uncover the populations of 4 endocrine cell types from the human islet bulk data despite the absence of many other cell types such as macrophages, Schwann cells and endothelial cells in the input single cell reference[20]. Although under such a circumstance, the absolute percentages of the cells remain obscure, we expect their relative proportions can be studied and valuable. A future improvement is to explicitly model the unknown cell types and estimate their percentages upon the signals in the compound data that cannot be explained by the contribution from the known components.

Methods

Gene selection

AdRoit selects genes that contain information about cell type identity, excluding non-informative genes that potentially introduce noise. There are two ways for selecting such genes: 1) union of the genes whose expression is enriched in one or more cell types in the single cell UMI count matrix. These genes are referred as marker genes; 2) union of the genes that vary the most across all the cells in the single cell UMI count matrix, referred as the highly variable genes. For marker genes, we recommend selecting top ~200 genes (P value < 0.05), ranked by fold change, from each cell type for resolving complex compound transcriptome data. Considering some genes may mark more than one cell types, we further require selected markers presenting in no more than 5 cell types to ensure specificity. We also suggest select a minimal of 1000 total number unique genes for an accurate estimation. If not satisfied, one may consider expand the number of top genes and/or loose the P value cutoff.

AdRoit also offer the option to use highly variable genes. To avoid the selected highly variable genes being dominated by large cell clusters whilst underrepresents small clusters, AdRoit first balances the cell types in the single cell UMI count matrix by finding the median size among all cell clusters, then sample cells from each cluster to make them equal to this size. Next, AdRoit computes the variance of each gene across the cells in the balanced single cell UMI matrix. Due to the well-known dispersion effect in RNA-seq data, directly computing variances from count matrix can results in overestimation. We thus compute variances on the normalized data done by variance-stabilizing transformation (VST)[51]. Genes with top 2000 large variances are then selected.

In both ways, mitochondria genes were excluded as their expression do not have information of cell identity. The results shown in current paper were based the marker genes as described above. But we also demonstrated that using the balanced highly variable genes yields comparably accurate estimations (Supplementary Fig. 6).

Estimate gene mean and dispersion per cell type

Modeling single cell RNA-seq data is challenging due to the cellular heterogeneity, technical sensitivity, and noise. While the expression of some genes can be not detected by chance, other genes may be found to be highly dispersed. These factors can lead to excessive variability even within the same cell type. AdRoit combats high noise and computational complexity by building models with estimated mean and dispersion per cell type. This strategy reduced the data complexity while preserve the cell type specific information.

Although typical analyses of RNA-seq data starts with normalization, Adroit does not do normalization prior to the mean estimation. Performing a normalization across all cell types forces every cell type to have the same amount of RNA transcripts, measured by the total unique molecular identifier (UMI) counts per cell. However, different cell types can have dramatically different amounts of transcripts. For example, the amount of RNA transcripts in neuronal cells is about 10 times fold of that in glial cells. Thus, normalization can falsely alter the relative abundance of cell types, misleading the estimation of cell type percentages. To avoid this problem, AdRoit models the means using the raw UMI counts.

Studies have shown that UMI counts follows negative binomial distribution[52,53], we therefore fit negative binomial distributions to single cells of each cell type and build the model based on the estimated means and dispersions from the selected genes. More specifically, let X_{ik}be the set of single cell UMI counts of gene $i \in 1,..,I$ for all cells in cell type $k \in 1, \dots, K$. I is the number of selected genes, and K denotes number of cell types in the single cell reference. The distribution of X_{ik}follows negative binomial distribution,

$$X_{ik} \sim NB(\lambda_{ik}, p_{ik}), \qquad (1)$$

where λ_{ik} is the dispersion parameter of the gene i in cell type k, and p_{ik} is the success probability, i.e., the probability of gene i in cell type k getting one UMI. The two parameters are estimated by MLE. The likelihood function is

$$LH(\lambda_{ik}, p_{ik}|X_{ik}) = \prod_{i=1}^{n_k} f(X_{ik}|\lambda_{ik}, p_{ik}), \qquad (2)$$

where n_k is the number of cells in cell type k, and f is the probability mass function of negative binomial distribution. The MLE estimates are then given by

$$(\widehat{\lambda_{ik}}, \widehat{p_{ik}}) = \underset{\lambda_{ik}, p_{ik}}{arg\max} LH(\lambda_{ik}, p_{ik}|X_{ik}). \qquad (3)$$

Once success probability and dispersion are estimated, the mean estimates can be computed numerically according to the property of negative binomial distribution,

$$\mu_{ik} = \frac{\widehat{\lambda_{ik}} \cdot \widehat{p_{ik}}}{1-\widehat{p_{ik}}}, \qquad (4)$$

$$\sigma_{ik}^2 = \frac{\widehat{\lambda_{ik}} \cdot \widehat{p_{ik}}}{(1-\widehat{p_{ik}})^2}. \qquad (5)$$

Estimation using MLE has been readily coded in many R packages. We choose ‘fitdist’ function from ‘fitdistrplus’ package[54] for its fast computation speed and flexibility in selecting distributions. Estimations are done for each selected gene in each cell type, resulting in a $I \times K$ matrix of cell type means.

Cell type specificity of genes

Genes with cell-type specific expression patterns better represent cell types, thus are more important when be used for resolving cell type composition. In line with this property, AdRoit weights genes with high specificity more than less specific ones. Highly specific genes usually have consistently high expression and thus relatively low variance among cells within a cell type. To compute cell type specificity of a gene, we first identify the cell type in which the gene has the highest expression (i.e., most specifically expressed cell type), then defines the specificity of this gene as the mean-to-variance ratio within the cell type. A high ratio renders high weight to the gene in the model. We use the estimated means and variances from negative binomial fitting (μ_{ik} and σ_{ik}^2 in eq. 4 and 5). Let k' be the index of cell type that has the highest mean expression of gene i,

$$k' = arg\max_{k}\{\mu_{ik} |\ k \,\epsilon\, 1 \dots K\}, \qquad (6)$$

then the cell type specificity weight for gene i, denoting w_i^S, is given by,

$$w_i^S = \frac{\mu_{ik'}}{\sigma_{ik'}^2}, \qquad (7)$$

and it is computed for each gene in the set of selected genes.

Cross-sample gene variability

The variability of a gene contrasts how much stable a gene is across samples. The idea of weighting genes based on variability across samples is first explored by Wang et al[22], where variability was defined as the cross-sample variance. By weighting down the high variability genes, the authors achieved a great advantage over the traditional unweighted method. Genes with low cross-sample variability better represent the population, hence are more trust-worthy to be used to learn the cell composition. AdRoit incorporates the same notion to weight the importance of genes, however, defines the variability in a more sophisticated way. Similar as we define the cell type specificity, AdRoit utilizes mean and variance, and computes variance-to-mean ratio (VMR) to stand for cross-sample gene variability. But here the mean and variance are computed across samples. The VMR is better scaled than the simple variance, and it can avoid underweighting genes that has low expression, while circumvent overweighting genes hugely dispersed.

In addition, AdRoit extends the method to fit the case where multiple samples are not available. We proposed three ways to compute the VMR, depending on whether multi-sample data is available. Typically, the compound transcriptome data to be deconvolved have multiple samples. In bulk RNA-seq data, multiple samples are usually included to control for biological variability. In spatial transcriptome data, the spatial dots can be seen as multiple samples. Therefore, we first consider computing the cross-sample gene variability from compound transcriptome data. In case multi-sample for compound data is not available, AdRoit utilizes the single cell reference, and synthesizes compound samples by pooling all cells belonging to the same sample. If multi-sample is not available for both data, AdRoit subsample single cells and pool them to make pseudo samples. Let Y_{ij} denote the counts of sequences for gene i in sample $j \in 1, \ldots, J$, then

$$Y_{ij} \sim NB(\lambda_{ij}, p_{ij}), \tag{8}$$

where λ_{ij} is the dispersion parameter of the gene i in sample j, and p_{ij} is the success probability. Again, we use MLE to get the estimates $\widehat{\lambda_{ij}}$and $\widehat{p_{ij}}$, following which cross-sample mean and variance can be numerically computed:

$$\mu_i^S = \frac{\widehat{\lambda_{ij}} \cdot \widehat{p_{ij}}}{1-\widehat{p_{ij}}}, \tag{9}$$

$$(\sigma_i^2)^S = \frac{\widehat{\lambda_{ij}} \cdot \widehat{p_{ij}}}{\left(1-\widehat{p_{ij}}\right)^2}, \tag{10}$$

and cross-sample variability for gene i is then defined as

$$VMR_i = \frac{(\sigma_i^2)^S}{\mu_i^S} = \frac{1}{w_i^C}, \tag{11}$$

where w_i^C is later used in the model. The cross-sample variability weight is computed for each gene in the set of selected genes.

Gene-wise scaling factor to correct platform bias

When linking the compound data to the single cell data, rescaling factor is often used to account for the library size and platform difference. The existing methods adopt a single rescaling factor for each unit of sample, i.e., all genes of a single sample are multiplied by the same factor[22,23]. This operation is based on a strong assumption that the impact of platform difference to every gene is the same and linearly scaled among different cell types, which is hardly true. In addition, because estimates can be easily affected by outliers in linear model, estimation of cell proportions can be steered away from the truth by extremely high expression genes. Therefore, applying a uniform scaling factor to all gene is inappropriate.

To overcome this problem, AdRoit instead estimates gene-wise scaling factors via an adaptive learning strategy and rescales each gene with its respective scaling factor. To proceed, we first input the mean gene expression from the compound samples (μ_i^Sin eq. 9) and the estimated means of each cell type from the single cell data (μ_{ik} in eq. 4), then apply a traditional non-negative least square regression (NNLS) to get a rough estimation of the proportions of each cell type, denoting τ_k. For each gene, a predicted mean expression ($\sum_k^K \widehat{\tau_k}\, \mu_{ik}$ in eq. 13) is computed as the weighted sum of the means of each cell type wherein the weights are the roughly estimated proportions. The regression equation is given by,

$$\mu_i^S = A \cdot \left(\sum_k^K \tau_k\, \mu_{ik} + \varepsilon\right), \qquad 0 < \tau_k,\ \sum_k^K \tau_k = 1 \qquad (12)$$

where A is a constant to ensure τ_k's sum to 1 and ε is the error term. We use 'nnls' function in the 'nnls' package[55] to estimate τ_k's. Next, we calculate the ratio between the mean expression from compound samples and the predicted means, and define the gene-wise rescaling factor as the logarithm of the ratio plus 1,

$$r_i = \log\left(\frac{\mu_i^s}{\sum_k^K \widehat{\tau_k} \mu_{ik}} + 1\right). \qquad (13)$$

Given the dispersion property of count data, the logarithm of the ratio is a more appropriate statistic as it results in relatively stable scaling factors. The addition of 1 avoids taking logarithm on zero. By multiplying the flexible gene-wise rescaling factor, the "outlier" genes will be pushed toward the truth regression line direction, while the genes around the true regression lines are less affected (Fig. 1b).

Weighted and regularized model

We next designed a model that incorporates all these factors to do the actual estimation of cell type proportions. AdRoit builds upon non-negative least square regression model. It gives high weights to the genes with high cell type specificity and low cross-sample variability. This was done by optimizing a weighted sum of squared loss function L, where the weights consist of two components (w_i^C in eq. 7, w_i^S in eq. 11). The gene-wise scaling factor tailored for each gene effectively corrects the bias due to technology difference between compound sample and single cell data ($r_i$in eq 13). In cases of complex tissues (e.g., neural tissues) where many highly similar subtypes are common, closely related subtypes can have strong collinearity, leading to overestimation of some cell types whilst underestimate or miss some others. AdRoit handles this problem by including a L2 norm of the estimates as the regularization component. Denote β_k as the unscaled coefficient for cell type k. For a compound transcriptome sample j, the loss function is given by,

$$L_j(\beta_1,\dots,\beta_K|y_{ij},w_i^C,w_i^S,r_i,\widehat{\mu_{ik}}) = \sum_i^I w_i^C \cdot w_i^S \cdot (y_{ij} - r_i \cdot \sum_k^K \beta_k \widehat{\mu_{ik}})^2 + \sum_k^K \beta_k^2. \quad (14)$$

Then the coefficient β_k can be estimated by minimizing the loss function with the constraint $\beta_1,\dots,\beta_K > 0$,

$$\widehat{\beta_1},\dots,\widehat{\beta_K} = \underset{\beta_1,\dots,\beta_K}{\mathrm{argmax}}_{\beta_1,\dots,\beta_K>0} L_j. \qquad (15)$$

The estimation is done by a gradient projection method by Byrd et al[56]. We derive the gradient function by taking partial derivative of the loss function with $w.r.t.$ β_k,

$$G_k = \nabla_{\beta_k} L_j = -2\sum_i^I r_i \cdot \widehat{\mu_{ik}} \cdot w_i^C \cdot w_i^S \cdot \left(y_{ij} - r_i \cdot \sum_k^K \beta_k \widehat{\mu_{ik}}\right) + 2\beta_k. \qquad (16)$$

AdRoit uses the function ‘optim’ from the R package ‘stats’ to do the estimation[57], providing the loss function (eq. 15) and the gradient (eq. 16). To get the final estimates of cell type proportions, we rescale the coefficients β_k’s to ensure a summation of 1,

$$\theta_k = \frac{\widehat{\beta_k}}{\sum_k^K \widehat{\beta_k}}. \qquad (17)$$

Each compound sample j is independently estimated by the model described above.

Simulation of bulk RNA-seq and spatial transcriptomics data

Bulk RNA-seq data used for benchmarking are synthesized by adding up the raw UMI reads per gene from all single cells of a sample regardless of cell types. Denote t_k as a cell in cell type k, and $t_k \in 1, \ldots, T_k$, where T_k is the number of cells in cell type k. Let Y_{ij}^B be the read count of gene i in a synthesized bulk sample j, and X_{ijt_k} be the UMI count of the gene, then

$$Y_{ij}^B = \sum_k^K \sum_{t_k}^{T_k} X_{ijt_k}.$$

The true proportion of cell type k is given by,

$$\theta_k^0 = \frac{T_k}{\sum_k^K T_k}.$$

To simulate spatial transcriptomic spots, we first sample 10 cells without replacement from each cell type and added them up, then mix them with designed proportions. For example, to simulate a spot with p_k percent of cell type k, the read count Y_{ij}^s of gene i in a spatial spot j is given by,

$$Y_{ij}^s = \sum_k^K p_k \sum_{n=1}^{10} X_{ikn},$$

where X_{iks} is UMI count of gene i in a sampled cell n of cell type k. For each mixing scheme, the simulation is repeated 100 times.

Evaluation statistics

We compared the estimated cell type proportions with the ground truth by calculating 4 statistics. The mAD and RMSD are given by,

$$mAD = \frac{\sum_k^K \left|\theta_k - \theta_k^0\right|}{K},$$

$$RMSD = \frac{\sum_k^K \left(\theta_k - \theta_k^0\right)^2}{K}.$$

Pearson correlation coefficient is computed as,

$$\rho_p = \frac{\sum_k^K (\theta_k - \overline{\theta_k})\left(\theta_k^0 - \overline{\theta_k^0}\right)}{\sqrt{\sum_k^K (\theta_k - \overline{\theta_k})^2}\sqrt{\sum_k^K \left(\theta_k^0 - \overline{\theta_k^0}\right)^2}},$$

where $\overline{\theta_k}$ and $\overline{\theta_k^0}$ are means of the estimated proportions and true proportions, respectively. Spearman correlation coefficient is given by,

$$\rho_s = \frac{\sum_k^K (r_k - \overline{r_k})\left(r_k^0 - \overline{r_k^0}\right)}{\sqrt{\sum_k^K (r_k - \overline{r_k})^2}\sqrt{\sum_k^K \left(r_k^0 - \overline{r_k^0}\right)^2}},$$

where $r_k$is the rank of θ_k.

Single cell RNA sequencing of mouse dorsal root ganglion

As described previously[58], lumbar DRGs were isolated from adult C57BL/6 mice and transferred to a dissociation buffer (Dulbecco's modified Eagle's medium supplemented with 10% heat-inactivated Fetal Calf Serum) (Gibco; cat # A38400-02). To generate a single cell suspension, DRGs were subjected to a 2 step-enzymatic dissociation followed by a mechanical dissociation.

In brief, DRGs were first incubated with 0.125% collagenase P from Clostridium histolyticum (Roche Applied Science; cat # 11249002001) for 90 minutes in an Eppendorf Thermomixer C (37°C; intermittent 750 rpm shaking for about 10 sec every 2 minutes). Then, DRGs were transferred to a Hank's Balanced Salt Solution (HBSS, Mg^{2+} and Ca^{2+} free; Invitrogen) supplemented with 0.25% Trypsin (Worthington biochemical corp.; cat # LSoo3707) and 0.0025% EDTA and incubated for 10 minutes at 37°C in the Eppendorf Thermomixer C. Trypsin was neutralized by the addition of 2.5 mg/ml MgSO4 (Sigma; cat #M-3937) and DRGs were triturated with Pasteur pipettes. The resulting cell suspension was passed through a 70 µm mesh filter to remove remaining chunks of tissues and centrifuged for 5 minutes at 2500 rpm at room temperature. The pellet was resuspended in HBSS ($Ca^{2+,}$ Mg^{2+} free; Invitrogen) and the cell suspension was run on a 30% Percoll Plus gradient (Sigma GE17-5445-02) to further remove debris. Finally, cells were resuspended in PBS supplemented with 0.04% BSA at a concentration of 200 cells/µl and cell viability was determined using the automated cell analyzer NucleoCounter® NC-250™. The suspended single cells were loaded on a Chromium Single Cell Instrument (10X Genomics) with about 6000 cells per lane to minimize the presence of doublets. 2000-3000 cells per lane were recovered. RNA-seq libraries were constructed using Chromium Single Cell 3' Library, Gel Beads & Multiplex Kit (10X Genomics). Single end sequencing was performed on Illumina NextSeq500. Read 1 starts with a 26-bp UMI and cell barcode, followed by an 8-bp i7 sample index. Read 2 contains a 55-bp transcript read. Sample de-multiplexing, alignment, filtering, and UMI counting were conducted using Cell Ranger Single-Cell Software Suite[59] (10X Genomics, v2.0.0). Mouse mm10 Genome assembly and UCSC gene model were used for the alignment.

Data preprocessing

DRG single cell data

The UMI data output from Cell Ranger Single-Cell Software Suite (10X Genomics, v2.0.0) was analyzed using Seurat package[60] to assess the cell quality and identify cell types, similar to what described previously[39]. Cells with the number of detected genes less than 500 or over 15000, or with a UMI ratio of mitochondria encoded genes versus all genes over 0.1 were also removed. The UMI data was normalized by the 'NormalizeData' method in Seurat with default settings. To avoid potential sample-to-sample variation caused by technical variation at various experiment steps, we employed Seurat data integration method. The top 2000 variable genes of each of the 5 samples were identified using 'FindVariableFeatures' with selection.method='vst'. Based on the union of these variable genes, the anchor cells in each sample were identified by 'FindIntegrationAnchors'. All the samples were then integrated by 'IntegrateData'. We subsequently scaled the integrated data ('ScaleData') and performed dimension reduction ('RunPCA'). Cells were then clustered based on the first 15 principal components by applying 'FindNeighbors' and 'FindClusters' (resolution=0.6, algorithm=1). Marker genes for each cluster were identified using 'FindAllMarkers'. Parameters were used such that these genes were expressed in at least 25% of the cells in the cluster, and on average 2-fold higher than the rest of cells with a multiple-testing adjusted Wilcoxon test p value of less than 0.01. The specificity of the canonical cell type-specific genes or cell cluster-specific genes were further examined by visualizations (Extended Data Fig. 2) and used to define the cell type for each cluster. At the end, the original UMI data from 17271 genes and 3352 cells that passed the quality control were organized into a matrix (genes as rows and cell identifiers as columns). This matrix, together with the cell type label for each cell therein, were loaded into AdRoit as reference profiles.

Mouse brain single cell data

The scRNA-seq reference data of the mouse brain were obtained from Zeisel et. al[32]. Among all the available data, we only retained 96,572 cells that were acquired from the brain regions, had an assigned cell type by the authors and a minimal total UMI of 1000. These cells corresponded to 183 clusters at the finest taxonomy level in the original study. As many of the clusters are highly similar, we decided to merge some of them to simplify the reference landscape. First, the top 50 cluster enriched markers were derived using Scanpy[61] via the 'rank_genes_groups' function (method='wilcoxon'), following the normalization ('normalize_per_cell'), log transformation ('log1p') and regressing out ('regress_out') the variances associated with the total UMI and the percentage of mitochondrial chromosome encoded genes per cell. Then, the pair-wise overlapping p-values among the clusters were calculated using the top 50 marker genes assuming the hypergeometric null distribution. Last, clusters with overlapping p-values more significant than 1e-10 were merged and new names were assigned by combinedly considering the original annotation, the molecular features and the specificity to certain brain regions. A total of 46 cell types were determined that cover all the 12 brain regions and their important substructures[37] (Supplementary Table 13). To make the reference dataset more manageable in size and more balanced in the representation of cell types, we down sampled each cluster to no more than 360 cells. A final set of 14,666 cells over 46 cell types were used for the deconvolution of the mouse brain spatial transcriptome data.

Human Islets

We used the 1492 high quality human islets single cell and annotation from Xin et al[38]. The RPKM expression table was directly downloaded and used as is. The RNA-FISH data was also from this study[38]. For the real bulk human pancreatic islets data[38,40,41], the read counts table were deconvoluted. Only data from donors with HbA1C level available were included in the regression of Beta cell proportion on HbA1C level (Fig. 4c, Supplementary Table 10).

Trabecular Meshwork

We downloaded the raw sequence data and followed the same analysis procedure as in Patel et al[39] for quality control and cell type identification.

Mouse Brain Spatial transcriptomics data by 10x Visium platform

The filtered cell matrix, tissue image and the spatial coordinates of a coronal section of an adult C57BL/6 mouse brain from the 10x Genomics were available for download and used as is.

Mouse Brian ISH images

The ISH images were directly downloaded from Allen mouse Brain Atlas[37] by searching the gene names. THE images were used with further editing except for cropping.

Data availability

DRG single cell data are deposited at NCBI GEO with accession number (to be added). The bulk RNA-seq and RNA-FISH data for human pancreatic islets were initially published as aggregated data where the data processing and experimental procedure were described therein[38,40,41]. We acquired the individual sample data from the authors and released them along with the current study (Supplementary Table 10 and Supplementary Table 12). The other public data analyzed in this study are available from: GEO (human pancreatic islets single cell data: GSE81608); NCBI (human trabecular meshwork single cell data: PRJNA616025; mouse brain single cell data: SRP135960). Mouse brain spatial transcriptomic data was downloaded from the 10x Genomics website (https://support.10xgenomics.com/spatial-gene-expression/datasets/1.1.0/V1_Adult_Mouse_Brain_Coronal_Section).

Code availability

AdRoit's source code is available on Github (https://github.com/TaoYang-dev/AdRoit).

Software

The statistical analyses were done with R statistical software (v3.6.0)[57] and python (v3.7.2)[62]. The packages used include Seurat (v3.0.1)[60], scanpy (v1.6.0)[61], dplyr (v0.8.0.1)[63], doParallel (v1.0.14)[64], data.table (v1.12.4)[65], fitdistrplus (v1.1-1)[54], nnls (v1.4)[55].

Reference

1. Wang, Z., Gerstein, M. & Snyder, M. RNA-Seq: A revolutionary tool for transcriptomics. *Nature Reviews Genetics* (2009) doi:10.1038/nrg2484.

2. Chu, G. C., Kimmelman, A. C., Hezel, A. F. & DePinho, R. A. Stromal biology of pancreatic cancer. *Journal of Cellular Biochemistry* (2007) doi:10.1002/jcb.21209.

3. Bussard, K. M., Mutkus, L., Stumpf, K., Gomez-Manzano, C. & Marini, F. C. Tumor-associated stromal cells as key contributors to the tumor microenvironment. *Breast Cancer Research* (2016) doi:10.1186/s13058-016-0740-2.

4. Munn, D. H. & Bronte, V. Immune suppressive mechanisms in the tumor microenvironment. *Current Opinion in Immunology* (2016) doi:10.1016/j.coi.2015.10.009.

5. Gonzalez, H., Hagerling, C. & Werb, Z. Roles of the immune system in cancer: From tumor initiation to metastatic progression. *Genes and Development* (2018) doi:10.1101/GAD.314617.118.

6. Garner, H. & de Visser, K. E. Immune crosstalk in cancer progression and metastatic spread: a complex conversation. *Nature Reviews Immunology* (2020) doi:10.1038/s41577-019-0271-z.

7. Singh, U. P. *et al.* Chemokine and cytokine levels in inflammatory bowel disease patients. *Cytokine* (2016) doi:10.1016/j.cyto.2015.10.008.

8. Van Lint, P. & Libert, C. Chemokine and cytokine processing by matrix metalloproteinases and its effect on leukocyte migration and inflammation. *J. Leukoc. Biol.* (2007) doi:10.1189/jlb.0607338.

9. Zelová, H. & Hošek, J. TNF-α signalling and inflammation: Interactions between old

acquaintances. *Inflammation Research* (2013) doi:10.1007/s00011-013-0633-0.

10. Koelman, L., Pivovarova-Ramich, O., Pfeiffer, A. F. H., Grune, T. & Aleksandrova, K. Cytokines for evaluation of chronic inflammatory status in ageing research: Reliability and phenotypic characterisation. *Immun. Ageing* (2019) doi:10.1186/s12979-019-0151-1.

11. Landskron, G., De La Fuente, M., Thuwajit, P., Thuwajit, C. & Hermoso, M. A. Chronic inflammation and cytokines in the tumor microenvironment. *Journal of Immunology Research* (2014) doi:10.1155/2014/149185.

12. Ståhl, P. L. *et al.* Visualization and analysis of gene expression in tissue sections by spatial transcriptomics. *Science* (2016) doi:10.1126/science.aaf2403.

13. Vickovic, S. *et al.* High-definition spatial transcriptomics for in situ tissue profiling. *Nat. Methods* (2019) doi:10.1038/s41592-019-0548-y.

14. Tang, F. *et al.* mRNA-Seq whole-transcriptome analysis of a single cell. *Nat. Methods* (2009) doi:10.1038/nmeth.1315.

15. Denisenko, E. *et al.* Systematic assessment of tissue dissociation and storage biases in single-cell and single-nucleus RNA-seq workflows. *Genome Biol.* (2020) doi:10.1186/s13059-020-02048-6.

16. Nguyen, Q. H., Pervolarakis, N., Nee, K. & Kessenbrock, K. Experimental considerations for single-cell RNA sequencing approaches. *Frontiers in Cell and Developmental Biology* (2018) doi:10.3389/fcell.2018.00108.

17. Tanay, A. & Regev, A. Scaling single-cell genomics from phenomenology to mechanism. *Nature* (2017) doi:10.1038/nature21350.

18. Abbas, A. R., Wolslegel, K., Seshasayee, D., Modrusan, Z. & Clark, H. F. Deconvolution of

blood microarray data identifies cellular activation patterns in systemic lupus erythematosus. *PLoS One* (2009) doi:10.1371/journal.pone.0006098.

19. Newman, A. M. *et al.* Robust enumeration of cell subsets from tissue expression profiles. *Nat. Methods* (2015) doi:10.1038/nmeth.3337.

20. Baron, M. *et al.* A Single-Cell Transcriptomic Map of the Human and Mouse Pancreas Reveals Inter- and Intra-cell Population Structure. *Cell Syst.* (2016) doi:10.1016/j.cels.2016.08.011.

21. Tsoucas, D. *et al.* Accurate estimation of cell-type composition from gene expression data. *Nat. Commun.* (2019) doi:10.1038/s41467-019-10802-z.

22. Wang, X., Park, J., Susztak, K., Zhang, N. R. & Li, M. Bulk tissue cell type deconvolution with multi-subject single-cell expression reference. *Nat. Commun.* (2019) doi:10.1038/s41467-018-08023-x.

23. Andersson, A. *et al.* Single-cell and spatial transcriptomics enables probabilistic inference of cell type topography. *Commun. Biol.* **3**, 565 (2020).

24. Newman, A. M. *et al.* Determining cell type abundance and expression from bulk tissues with digital cytometry. *Nat. Biotechnol.* (2019) doi:10.1038/s41587-019-0114-2.

25. Myung, I. J. Tutorial on maximum likelihood estimation. *J. Math. Psychol.* (2003) doi:10.1016/S0022-2496(02)00028-7.

26. Bassett, R. & Deride, J. Maximum a posteriori estimators as a limit of Bayes estimators. *Math. Program.* (2019) doi:10.1007/s10107-018-1241-0.

27. Zhao, Y. & Simon, R. Gene expression deconvolution in clinical samples. *Genome Medicine* (2010) doi:10.1186/gm214.

28. Chiu, Y. J., Hsieh, Y. H. & Huang, Y. H. Improved cell composition deconvolution method of bulk gene expression profiles to quantify subsets of immune cells. *BMC Med. Genomics* (2019) doi:10.1186/s12920-019-0613-5.

29. Kang, K. *et al.* CDSeq: A novel complete deconvolution method for dissecting heterogeneous samples using gene expression data. *PLoS Comput. Biol.* (2019) doi:10.1371/journal.pcbi.1007510.

30. Qiao, W. *et al.* PERT: A Method for Expression Deconvolution of Human Blood Samples from Varied Microenvironmental and Developmental Conditions. *PLoS Comput. Biol.* (2012) doi:10.1371/journal.pcbi.1002838.

31. Zaitsev, K., Bambouskova, M., Swain, A. & Artyomov, M. N. Complete deconvolution of cellular mixtures based on linearity of transcriptional signatures. *Nat. Commun.* (2019) doi:10.1038/s41467-019-09990-5.

32. Zeisel, A. *et al.* Molecular Architecture of the Mouse Nervous System. *Cell* (2018) doi:10.1016/j.cell.2018.06.021.

33. Donovan, M. K. R., D'Antonio-Chronowska, A., D'Antonio, M. & Frazer, K. A. Cellular deconvolution of GTEx tissues powers discovery of disease and cell-type associated regulatory variants. *Nat. Commun.* (2020) doi:10.1038/s41467-020-14561-0.

34. Phipson, B., Zappia, L. & Oshlack, A. Gene length and detection bias in single cell RNA sequencing protocols. *F1000Research* (2017) doi:10.12688/f1000research.11290.1.

35. Chen, G., Ning, B. & Shi, T. Single-cell RNA-seq technologies and related computational data analysis. *Frontiers in Genetics* (2019) doi:10.3389/fgene.2019.00317.

36. Chen, D. & Plemmons, R. J. Nonnegativity constraints in numerical analysis. in *The Birth*

of Numerical Analysis (2009). doi:10.1142/9789812836267_0008.

37. Lein, E. S. *et al.* Genome-wide atlas of gene expression in the adult mouse brain. *Nature* (2007) doi:10.1038/nature05453.

38. Xin, Y. *et al.* RNA Sequencing of Single Human Islet Cells Reveals Type 2 Diabetes Genes. *Cell Metab.* (2016) doi:10.1016/j.cmet.2016.08.018.

39. Patel, G. *et al.* Molecular taxonomy of human ocular outflow tissues defined by single-cell transcriptomics. *Proc. Natl. Acad. Sci.* **117**, 12856 LP – 12867 (2020).

40. Xin, Y. *et al.* Pseudotime ordering of single human B-cells reveals states of insulin production and unfolded protein response. *Diabetes* (2018) doi:10.2337/db18-0365.

41. Gutierrez, G. D. *et al.* Gene signature of proliferating human pancreatic a cells. *Endocrinology* (2018) doi:10.1210/en.2018-00469.

42. Cerf, M. E. Beta cell dysfunction and insulin resistance. *Frontiers in Endocrinology* (2013) doi:10.3389/fendo.2013.00037.

43. Maedler, K. & Donath, M. Y. Beta-cells in type 2 diabetes: a loss of function and mass. *Hormone research* (2004).

44. Donath, M. Y. *et al.* Mechanisms of β-cell death in type 2 diabetes. *Diabetes* (2005) doi:10.2337/diabetes.54.suppl_2.S108.

45. Calanna, S. *et al.* Alpha- and beta-cell abnormalities in haemoglobin A1c-defined prediabetes and type 2 diabetes. *Acta Diabetol.* (2014) doi:10.1007/s00592-014-0555-5.

46. Kanat, M. *et al.* The Relationship Between β-Cell Function and Glycated Hemoglobin. *Diabetes Care* **34**, 1006 LP – 1010 (2011).

47. Nepton, S. Beta-Cell Function and Failure. in *Type 1 Diabetes* (2013). doi:10.5772/52153.

48. Dolenšek, J., Rupnik, M. S. & Stožer, A. Structural similarities and differences between the human and the mouse pancreas. *Islets* (2015) doi:10.1080/19382014.2015.1024405.

49. Lein, E. S. *et al.* Genome-wide atlas of gene expression in the adult mouse brain. *Nature* **445**, 168–176 (2007).

50. Vieth, B., Parekh, S., Ziegenhain, C., Enard, W. & Hellmann, I. A systematic evaluation of single cell RNA-seq analysis pipelines. *Nat. Commun.* (2019) doi:10.1038/s41467-019-12266-7.

51. Anders, S. & Huber, W. Differential expression analysis for sequence count data. *Genome Biol.* (2010) doi:10.1186/gb-2010-11-10-r106.

52. Hafemeister, C. & Satija, R. Normalization and variance stabilization of single-cell RNA-seq data using regularized negative binomial regression. *Genome Biol.* (2019) doi:10.1186/s13059-019-1874-1.

53. Svensson, V. Droplet scRNA-seq is not zero-inflated. *Nature Biotechnology* (2020) doi:10.1038/s41587-019-0379-5.

54. Delignette-Muller, M. L. & Dutang, C. fitdistrplus: An R package for fitting distributions. *J. Stat. Softw.* (2015) doi:10.18637/jss.v064.i04.

55. Mullen, Katharine M., I. H. M. van S. nnls: The Lawson-Hanson algorithm for non-negative least squares (NNLS). *R Packag. version 1.4* (2012).

56. Byrd, R. H., Lu, P., Nocedal, J. & Zhu, C. A Limited Memory Algorithm for Bound Constrained Optimization. *SIAM J. Sci. Comput.* (1995) doi:10.1137/0916069.

57. The R Core Team. R: A Language and Environment for Statistical Computing. *R Foundation for Statistical Computing* (2019).

58. Alessandri-Haber, N. *et al.* Hypotonicity induces TRPV4-mediated nociception in rat. *Neuron* (2003) doi:10.1016/S0896-6273(03)00462-8.

59. Zheng, G. X. Y. *et al.* Massively parallel digital transcriptional profiling of single cells. *Nat. Commun.* (2017) doi:10.1038/ncomms14049.

60. Stuart, T. *et al.* Comprehensive Integration of Single-Cell Data. *Cell* (2019) doi:10.1016/j.cell.2019.05.031.

61. Wolf, F. A., Angerer, P. & Theis, F. J. SCANPY: Large-scale single-cell gene expression data analysis. *Genome Biol.* (2018) doi:10.1186/s13059-017-1382-0.

62. van Rossum, G. & Drake, F. L. *Python 3 Reference Manual. Scotts Valley, CA* (2009).

63. Wickham, H. & Francois, R. dplyr: A Grammar of Data Manipulation. *R Packag. version 0.4.2.* (2015).

64. Weston, S., Calaway, R. & Tenenbaum, D. *doParallel: Foreach Parallel Adaptor for the Parallel Package*. *Cran* (2014).

65. Dowle, M. & Srinivasan, A. data.table: Extension of 'data.frame'. R Package Version 1.12.8. *Manual* (2019).

Acknowledgements

We thank Yurong Xin for pointing us to the relevant public data resource. We also thank Gabor Halasz and Yuan Zhu for the advice to algorithm design.

Author contributions

T.Y., Y.B., W.F., N. A.-H., M. L.-F., L. E.M. and G. S. A. designed the research. T.Y., Y.B., and W.F. developed the algorithm. T.Y., Y.B., W.F. and J.K. participated in the data analyzing. M.S. and R.B. performed the DRG tissue collection. C.A. performed the single cell library preparation and sequencing experiment. T.Y., Y.B., N.A.-H. and G. S. A. wrote the manuscript.

Competing interests

T.Y., Y.B., W.F. and G.S.A. have filed a patent application relating to the AdRoit computational framework. All authors are employees and shareholders of Regeneron Pharmaceuticals, although the manuscript's subject matter does not have any relationship to any products or services of this corporation.

Figure legends

Fig. 1: Schematic representation of AdRoit computational framework. a, AdRoit inputs bulk or spatial RNA-seq data, single cell RNA-seq data and cell type annotations. It first selects informative genes and estimates their means and dispersions, based on which the cell type specificity of genes is computed. Depending on multi-sample availability, cross-sample gene variability is estimated from compound data, or single cell samples (dashed arrow). Lastly the gene-wise scaling factors are estimated using both compound data and single cell data. These computed quantities are fed to a weighted regularized model to infer the transcriptome composition. **b,** A mock example to illustrate the role of gene-wise scaling factor. Ideally, an accurate estimation of slop (i.e., cell proportion) would be the slope of the green line, however direct fitting would result in the red line due to the impact of the outlier genes. Outlier genes

can be induced due to platform difference affecting genes differently. AdRoit adopts an adaptive learning approach that first learns a rough estimation of the slop (red line), then moves the outlier genes toward it such that the more deviated genes will be moved more toward the true line (i.e., longer arrows). After the adjustment, the new estimated slop (blue line) is closer to the truth (green line), thus is a more accurate estimation.

Fig.2: Benchmark on simulated bulk data synthesized from trabecular meshwork (TM) single cells data. a, AdRoit has the closest estimation to the true cell proportion comparing to MuSiC and NNLS. Each dot is a cell type from one donor. **b,** For each cell type in TM, AdRoit has the smallest differences from the true cell type proportion and the smallest variance of estimates across the 8 donors. For each cell type, a dot on the graph denotes a donor, and the bars represent the $1.5\ \times$ interquartile ranges. Estimation was done by using the single cell as reference leaving out the donor used for synthesizing bulk. **c,** AdRoit's estimates are more accurate and specific than MuSiC's estimates on synthetic bulk that contains partial cell types. The synthetic bulk was simulated by using only 6 out of the 12 cell types per donor, then estimated with the reference of 12 cell types. AdRoit has notably fewer false positive estimates of the 6 cell types not included, and more accurate estimation of the 6 cell types used for synthesizing bulk. **d,** Receiver operating characteristic (ROC) curve shows AdRoit has a significantly higher AUC than MuSiC (0.95 vs 0.74), meaning better sensitivity and specificity.

Fig. 3: Benchmark on scRNA-seq data from dorsal root ganglion (DRG) where these exist many closely related subtypes of neuronal cells. a, 14 cell types were identified from scRNA-seq

samples of 5 mice, including multiple subtypes of neurofilaments (NF), peptidergic (PEP) and non-peptidergic (NP) neurons. **b,** Benchmarking with the synthetic data shows AdRoit's estimation of cell type proportions are highly accurate. In particular, AdRoit achieves reasonably high accuracy when the cells are rare (e.g., < 5%). Each dot represents a cell type from one sample. **c,** For each individual sample, mAD, RMSD, Pearson and Spearman correlations were computed and compared across three methods. AdRoit has the lowest mAD and RMSD, and highest Pearson and Spearman correlations. In addition, AdRoit's estimation is also the most stable across samples. Each dot on the boxplot is a sample. Estimation was done by using the single cell reference leaving out the sample used for synthesizing bulk.

Fig. 4: AdRoit is more accurate and sensitive than Stereoscope on spatial spots simulated from real DRG cells. a, AdRoit and Stereoscope estimations on simulated spatial spots that contains 5 PEP neuron subtypes. True mixing proportions were denoted by the red dashed lines. Three schemes were simulated: 1) the proportions of 5 PEP cell types are the same and equal to 0.2; 2) PEP1_Dcn is 0.1 and the other 4 are 0.225; 3) PEP1_Dcn and PEP1_S100a11.Tagln2 are 0.1, PEP1_Slc7a3.Sstr2 and PEP2_Htr3a.Sema5a 0.2 are 0.2, and PEP3_Trpm8 is 0.4. In all simulation schemes, AdRoit's estimates are more consistently centered around the true proportions than Stereoscope's estimates. **b,** AdRoit is more accurate in estimating rare cells in spatial spots. The spots were simulated by simulating mixtures of 3 PEP cell types (i.e., PEP1_Slc7a3.Sstr2, PEP2_Htr3a.Sema5a and PEP3_Trpm8), with a series of low percent of PEP3_Trpm8 cell type from 1% to 10% and the other two cell types sharing the rest proportion equally. AdRoit's estimates are systematically closer to the true simulated

proportions than Stereoscope's estimates. **c,** AdRoit is consistently more sensitive than Stereoscope in detecting low percent cells (estimates > 0.5% deemed as detected) in simulated spots of 1) low percent of NF_Calb1 mixed with NF_Pvalb and NF2_Ntrk2.Necab2, 2) low percent of NP_Mrgpra3 mixed with NP_Mrgprd and NP_Nts, 3) low percent of PEP3_Trpm8 mixed with PEP1_Slc7a3.Sstr2 and PEP2_Htr3a.Sema5a, 4) low percent of NF_Calb1 mixed with Th, satellite glia and endothelial, 5) low percent of NP_Mrgpra3 mixed with Th, satellite glia and endothelial, and 6) low percent of PEP_Trpm8 mixed with Th, satellite glia and endothelial.

Fig. 5: Applications to real bulk human islets RNA-seq data and mouse brain spatial transcriptome data. a, AdRoit's estimates on real human Islets bulk RNA-seq data were highly reproducible for the repeated samples from same donor. **b,** AdRoit estimated cell type proportions agreed with the RNA-FISH measurements. **c,** AdRoit estimated Beta cell proportions in type 2 diabetes patients are significantly lower than that in healthy subjects. In addition, the estimated proportions have a significant negative linear association with donors' HbA1C level. **d,** The spatial mapping of 4 mouse brain cell types is consistent with the ISH images of 4 marker genes from Allen mouse brain atlas[37] respectively. The 4 genes, Spink8 (marker of hippocampal field CA1), C1ql2 (marker of Dentate Gyrus), Clic6 (marker of Choroid Plexus), Synpo2 (marker of Thalamus) were identified as markers of corresponding tissues by Zeisel et al[32].

Extended Data Fig. 1: Benchmark three methods on human pancreatic islets data. a, Human islets single cell data contains 4 cell types from 18 subjects including two major cell types Alpha and Beta cells, and two minor cells PP and Delta cells[38]. The cell proportion varies across different subjects. **b, c,** AdRoit achieves leading accuracy when applied to the bulk data synthesized from the single cell data. Each dot on scatterplot is a cell type from one subject. Estimation was done by using the single cell reference leaving out the subject used to synthesize bulk.

Extended Data Fig. 2: Dorsal root ganglion single cell shows 14 cell types including 3 subtypes of neurofilament, 3 subtypes of non-peptidergic neurons, and 5 subtypes of peptidergic neurons. a, Heatmap of top markers shows distinction between cell types as well as similarity between subtypes. **b,** The proportion of each cell type varies from 0.5% to 33.71% across different samples.

Extended Data Fig. 3: Comparing the performance on estimated simulated spatial spots of 14 pure cell type respectively. a, Estimates by AdRoit and **b,** estimates by Stereoscope are comparably accurate. Simulations were done by sampling cells from the same cell type and adding up the read counts per gene. For each of the 14 cell types of the DRG tissue, we repeated the simulation 100 times. The results shown were a summary of 100 simulations for each cell type. For both methods, the median estimates of the sampled cell type were close to 1 (red lines), whereas the cell type not sampled has zero or close-to-zero values.

Extended Data Fig. 4: The comparison of AdRoit and Stereoscope on the simulated spots of additional cell mixing schemes. 5 more types of mixed spatial spots were simulated: 1) mixture of 3 neurofilaments (NF); 2) mixture of 3 non-peptidergic (NP) cell types; 3) NF2_Ntrk2.Necab2 mixing with Th, satellite glia and endothelial; 4) NP_Nts mixing with Th, satellite glia and endothelial; and 5) PEP3_Trpm8 mixing with Th, satellite glia and endothelial. Each simulation was repeated 100 times. Consistently for all simulation schemes, AdRoit's estimates were always closer to the true simulated proportions (red lines), whereas Stereoscope's estimates largely deviated from the true proportions.

Extended Data Fig. 5: Spatial mapping of 46 cell types with AdRoit quantitative depicts the content in each spot. Spatial transcriptomics data was downloaded from 10x genomics (https://support.10xgenomics.com/spatial-gene-expression/datasets/1.1.0/V1_Adult_Mouse_Brain_Coronal_Section). The reference single cells were sampled from Zeisel et al[32] and curated into 46 cell types.

Figures

Fig. 1

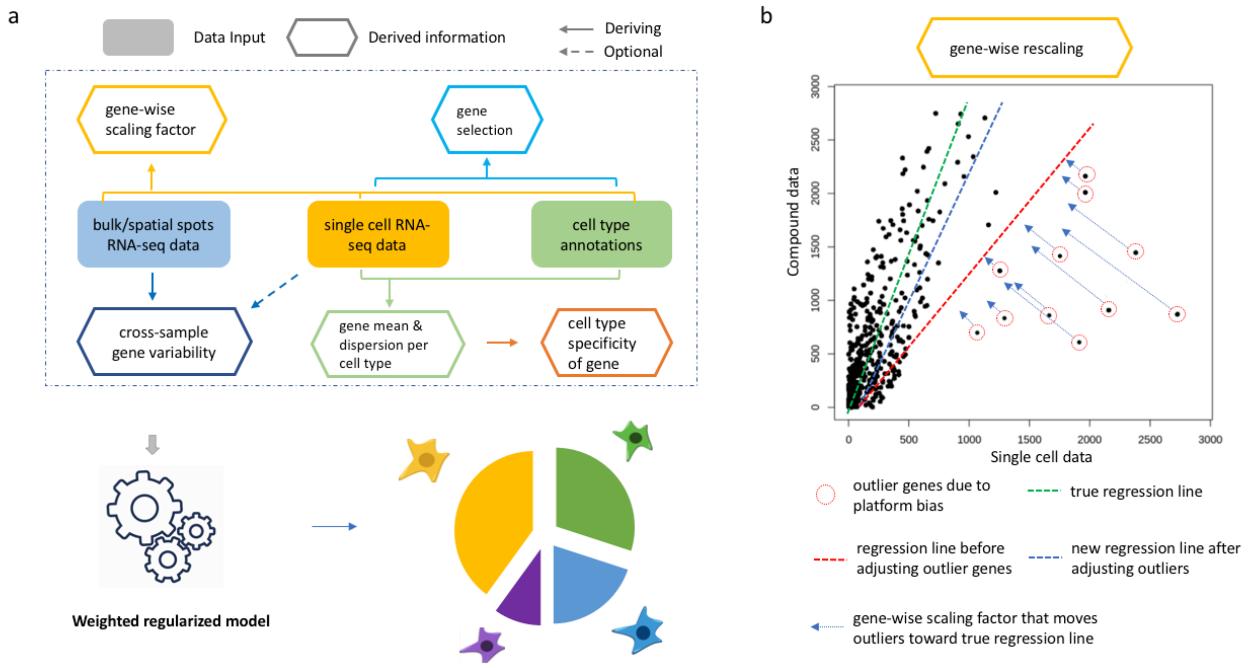
a
Data Input
Derived information
Deriving
Optional
gene-wise scaling factor
gene selection
bulk/spatial spots RNA-seq data
single cell RNA-seq data
cell type annotations
cross-sample gene variability
gene mean & dispersion per cell type
cell type specificity of gene
Weighted regularized model
b
gene-wise rescaling
Compound data
Single cell data
0
500
1000
1500
2000
2500
3000
outlier genes due to platform bias
true regression line
regression line before adjusting outlier genes
new regression line after adjusting outliers
gene-wise scaling factor that moves outliers toward true regression line

Fig. 2

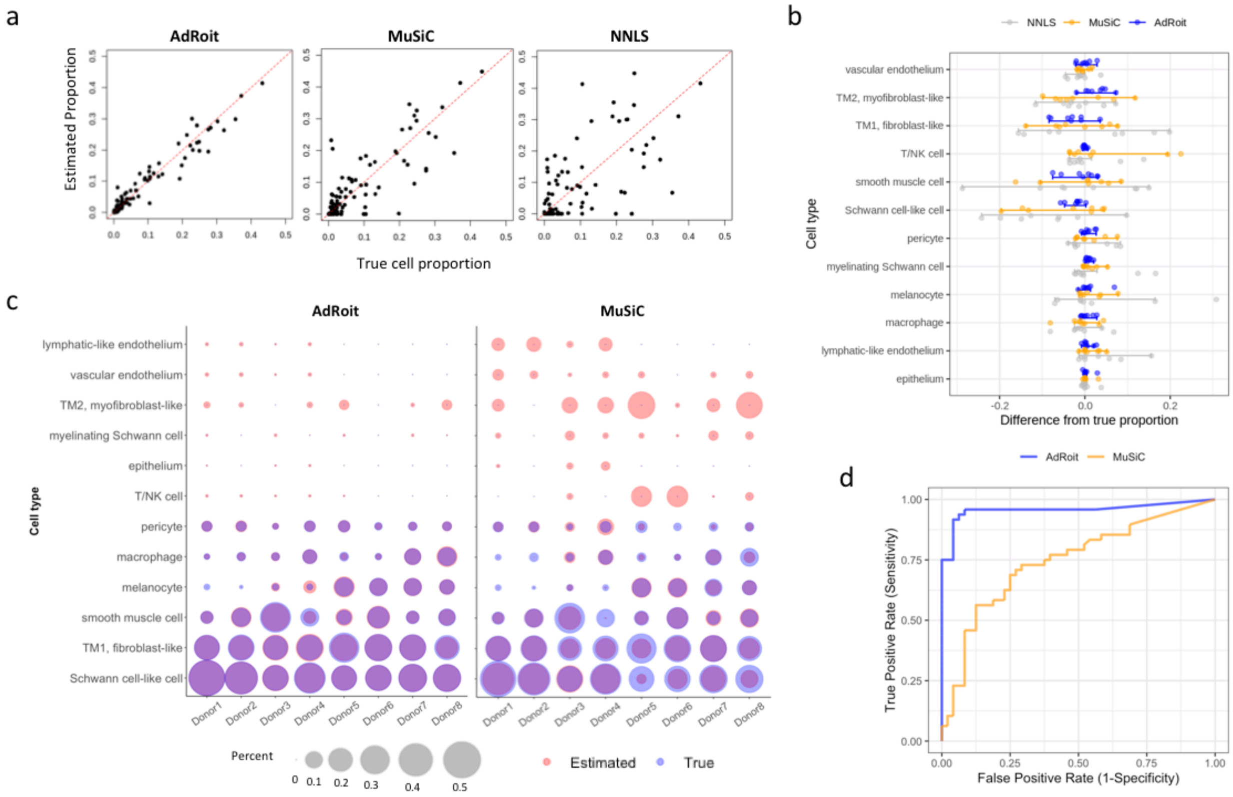
a
AdRoit
MuSiC
NNLS
Estimated Proportion
True cell proportion
0.0
0.1
0.2
0.3
0.4
0.5
b
NNLS
MuSiC
AdRoit
Cell type
vascular endothelium
TM2, myofibroblast-like
TM1, fibroblast-like
T/NK cell
smooth muscle cell
Schwann cell-like cell
pericyte
myelinating Schwann cell
melanocyte
macrophage
lymphatic-like endothelium
epithelium
-0.2
0.0
0.2
Difference from true proportion
c
AdRoit
MuSiC
Cell type
lymphatic-like endothelium
vascular endothelium
TM2, myofibroblast-like
myelinating Schwann cell
epithelium
T/NK cell
pericyte
macrophage
melanocyte
smooth muscle cell
TM1, fibroblast-like
Schwann cell-like cell
Donor1
Donor2
Donor3
Donor4
Donor5
Donor6
Donor7
Donor8
Percent
0
0.1
0.2
0.3
0.4
0.5
Estimated
True
d
AdRoit
MuSiC
True Positive Rate (Sensitivity)
False Positive Rate (1-Specificity)
0.00
0.25
0.50
0.75
1.00

Fig. 3

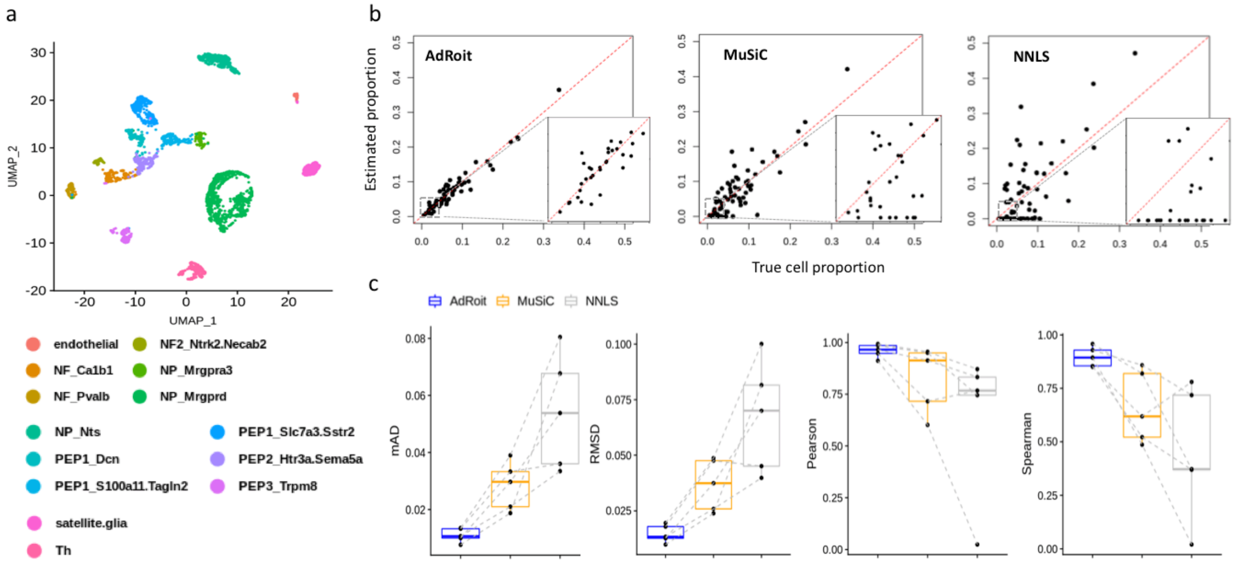
a
UMAP_2
UMAP_1
endothelial
NF2_Ntrk2.Necab2
NF_Calb1
NP_Mrgpra3
NF_Pvalb
NP_Mrgprd
NP_Nts
PEP1_Slc7a3.Sstr2
PEP1_Dcn
PEP2_Htr3a.Sema5a
PEP1_S100a11.Tagln2
PEP3_Trpm8
satellite.glia
Th
b
AdRoit
MuSiC
NNLS
Estimated proportion
True cell proportion
c
AdRoit
MuSiC
NNLS
mAD
RMSD
Pearson
Spearman

Fig. 4

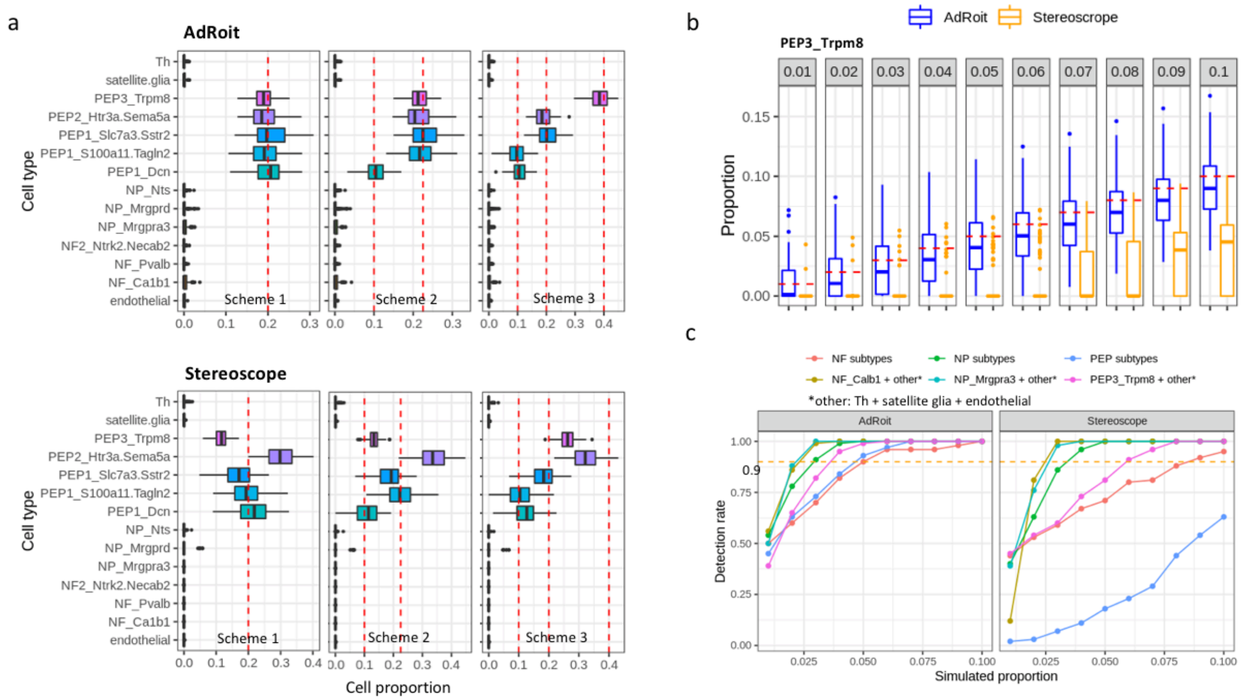
a
AdRoit
Th
satellite.glia
PEP3_Trpm8
PEP2_Htr3a.Sema5a
PEP1_Slc7a3.Sstr2
PEP1_S100a11.Tagln2
PEP1_Dcn
NP_Nts
NP_Mrgprd
NP_Mrgpra3
NF2_Ntrk2.Necab2
NF_Pvalb
NF_Calb1
endothelial
Cell type
Scheme 1
Scheme 2
Scheme 3
0.0 0.1 0.2 0.3
0.0 0.1 0.2 0.3
0.0 0.1 0.2 0.3 0.4
Stereoscope
0.0 0.1 0.2 0.3 0.4
Cell proportion
b
AdRoit
Stereoscope
PEP3_Trpm8
0.01 0.02 0.03 0.04 0.05 0.06 0.07 0.08 0.09 0.1
Proportion
0.00 0.05 0.10 0.15
c
NF subtypes
NP subtypes
PEP subtypes
NF_Calb1 + other*
NP_Mrgpra3 + other*
PEP3_Trpm8 + other*
*other: Th + satellite glia + endothelial
AdRoit
Stereoscope
Detection rate
0.00 0.25 0.50 0.75 0.9 1.00
0.025 0.050 0.075 0.100
Simulated proportion

Fig. 5

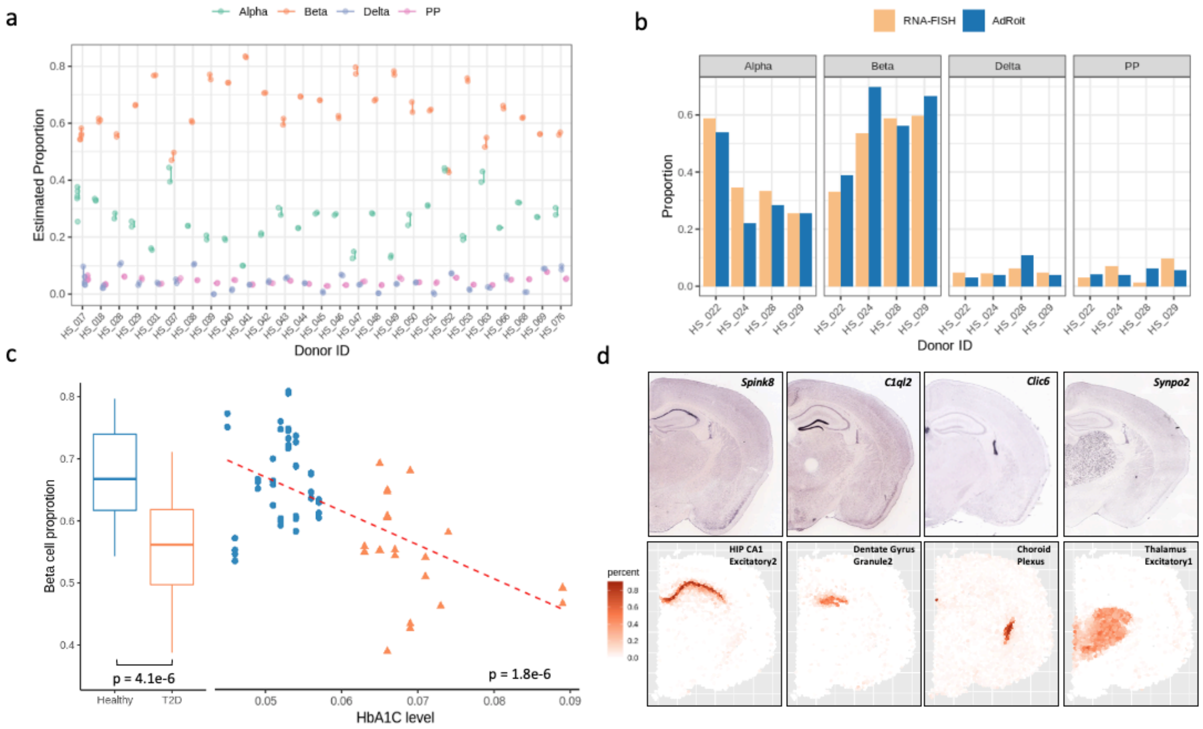
a
Alpha
Beta
Delta
PP
Estimated Proportion
0.0
0.2
0.4
0.6
0.8
HS_017
HS_018
HS_028
HS_029
HS_031
HS_037
HS_038
HS_039
HS_040
HS_041
HS_042
HS_043
HS_044
HS_045
HS_046
HS_047
HS_048
HS_049
HS_050
HS_051
HS_052
HS_053
HS_063
HS_066
HS_068
HS_069
HS_076
Donor ID
b
RNA-FISH
AdRoit
Alpha
Beta
Delta
PP
Proportion
0.0
0.2
0.4
0.6
HS_022
HS_024
HS_028
HS_029
Donor ID
c
Beta cell proportion
0.4
0.5
0.6
0.7
0.8
p = 4.1e-6
Healthy
T2D
p = 1.8e-6
0.05
0.06
0.07
0.08
0.09
HbA1C level
d
Spink8
C1ql2
Clic6
Synpo2
percent
0.8
0.6
0.4
0.2
0.0
HIP CA1 Excitatory2
Dentate Gyrus Granule2
Choroid Plexus
Thalamus Excitatory1

Extended Data Fig. 1

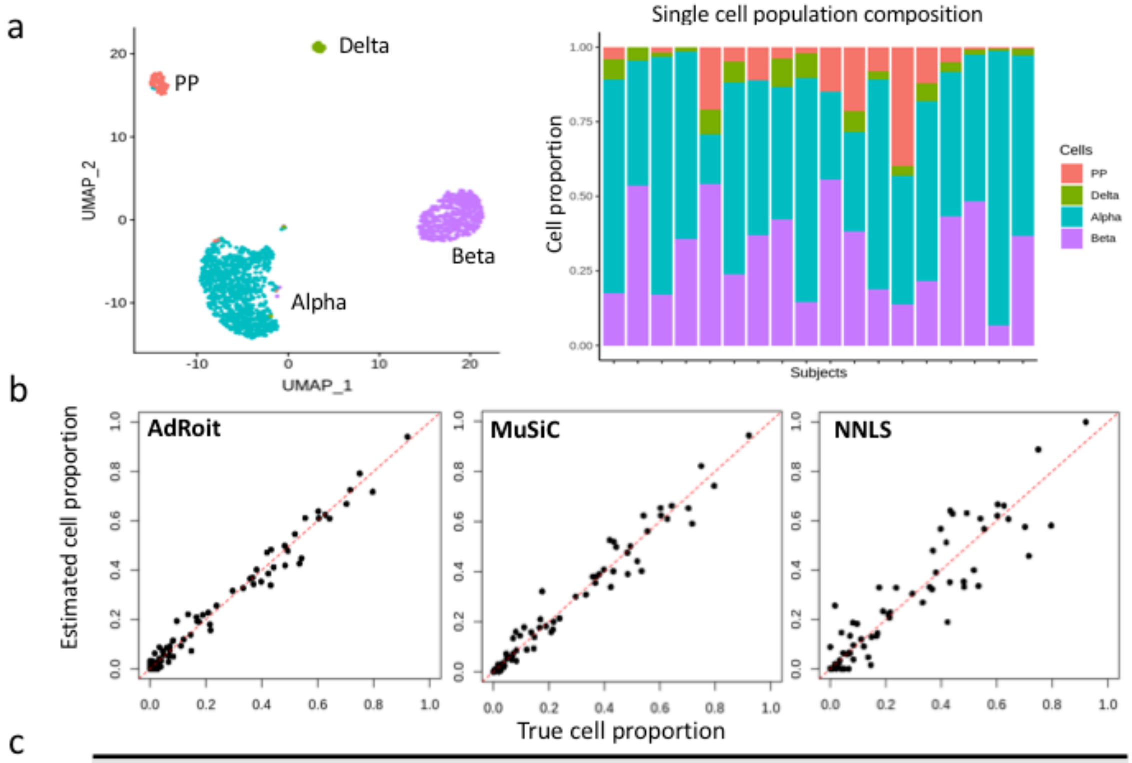

c

	AdRoit	MuSiC	NNLS
mAD	0.029	0.031	0.066
RMSD	0.039	0.046	0.095
Pearson	0.99	0.98	0.93
Spearman	0.97	0.98	0.91

Extended Data Fig. 2

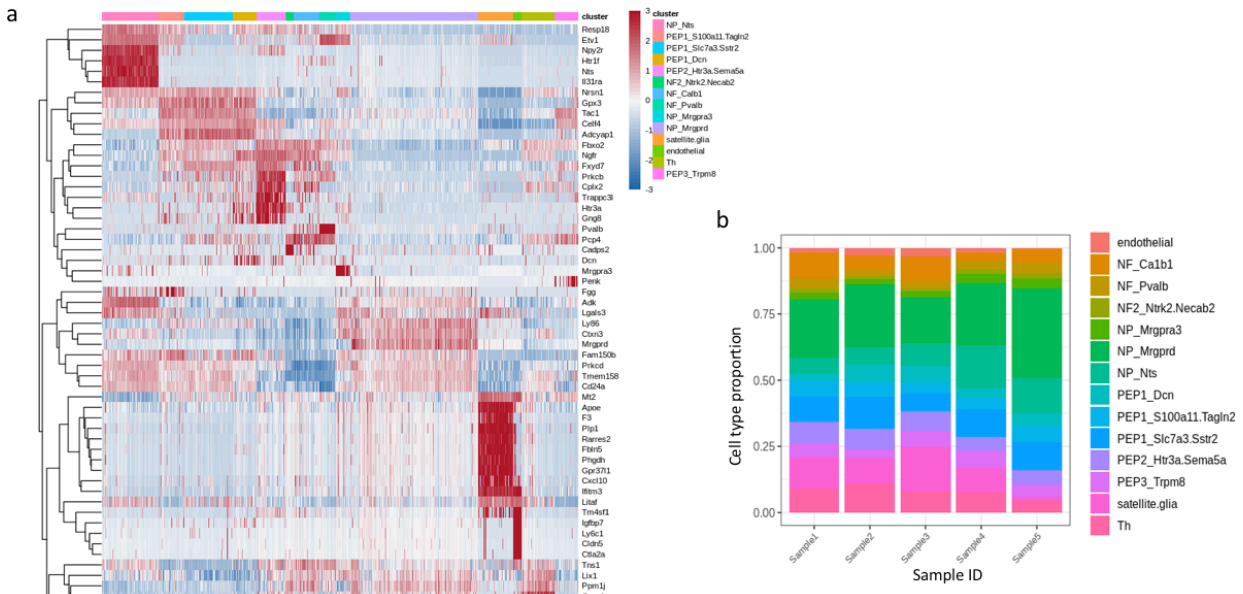

Extended Data Fig. 3

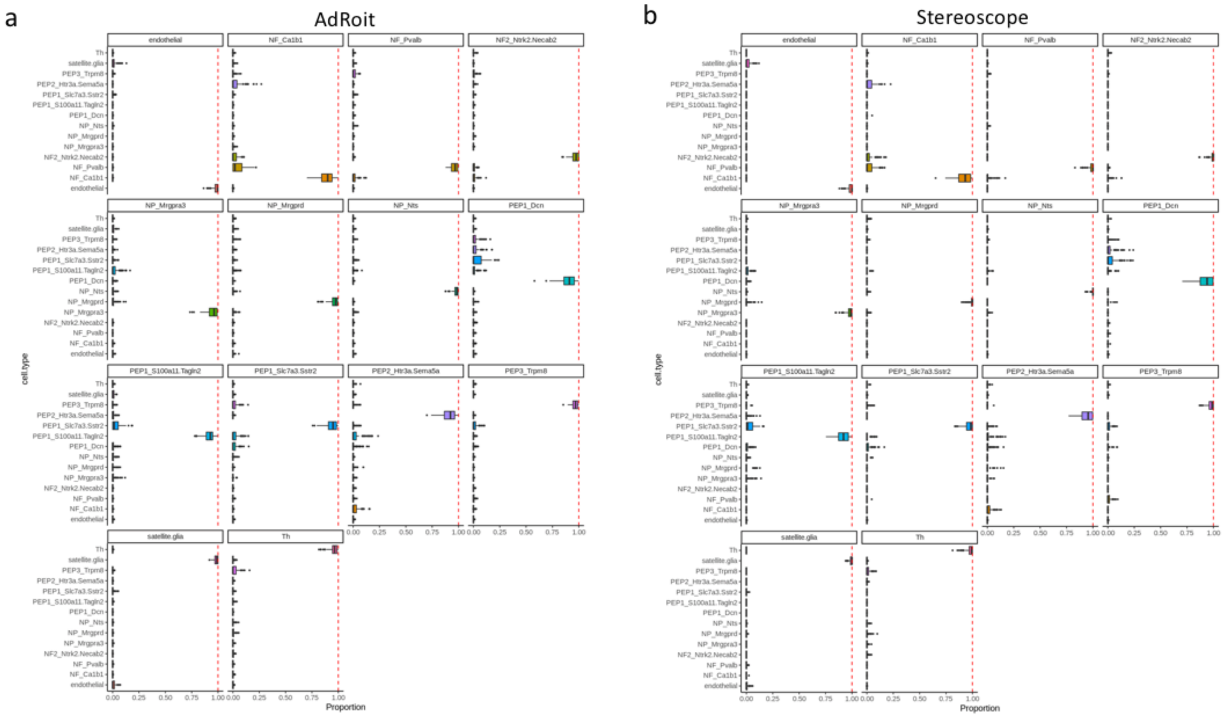

Extended Data Fig. 4

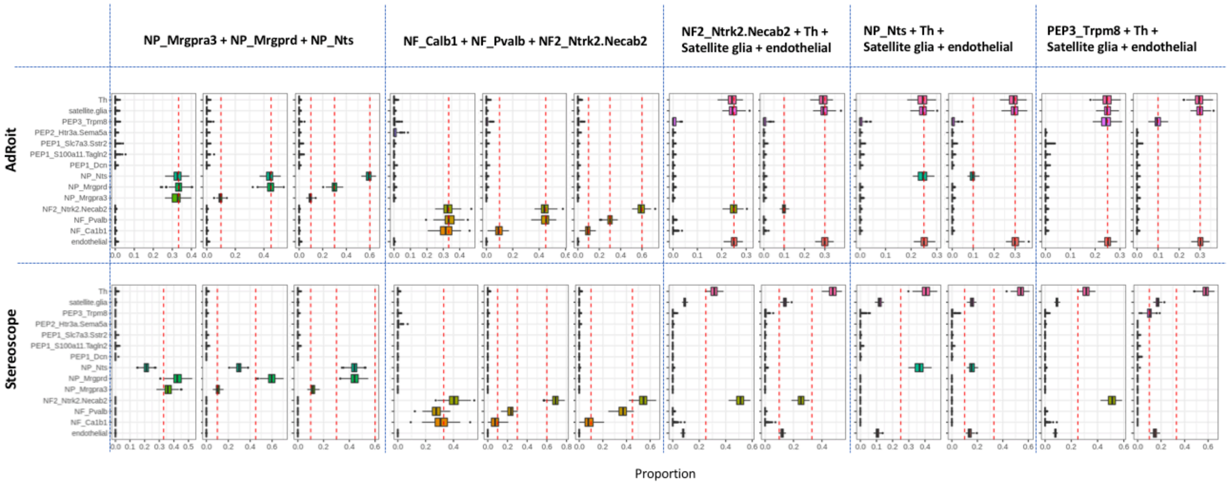

1212 **Extended Data Fig. 5**

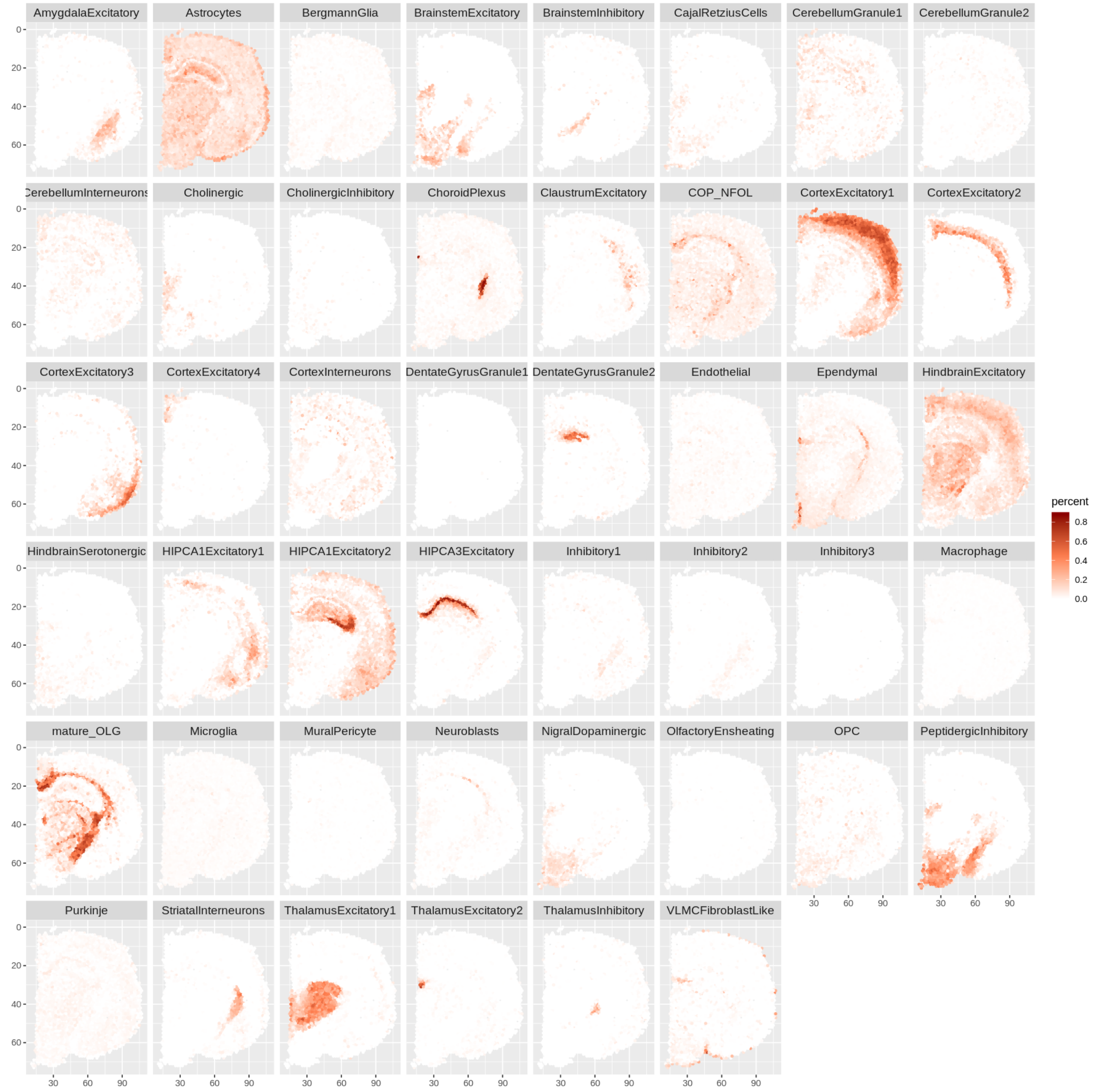

1213

1214

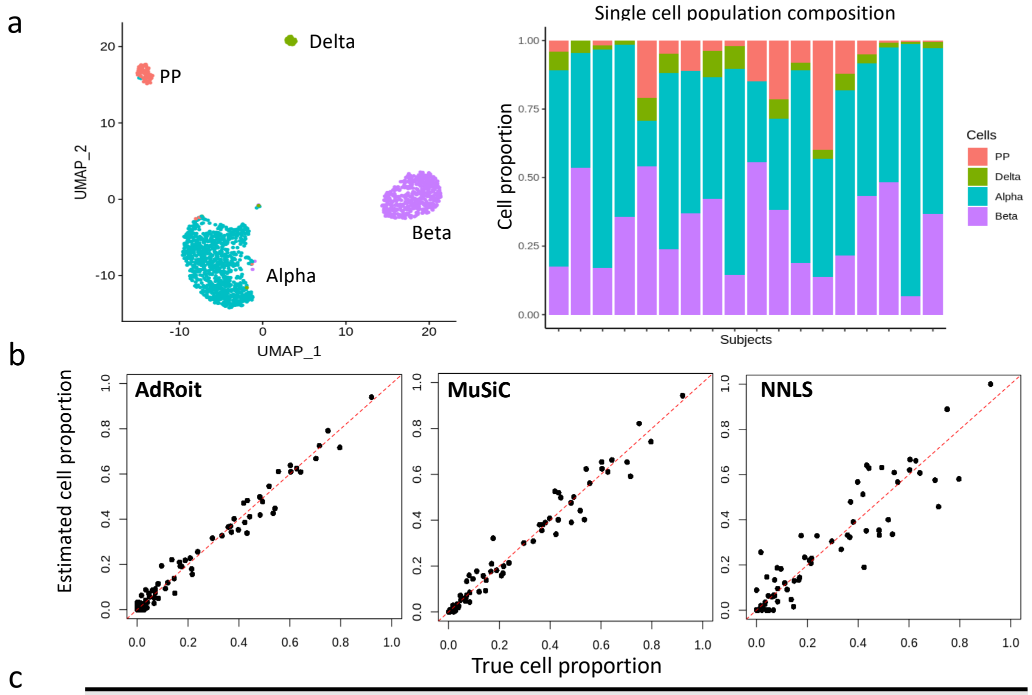

c

	AdRoit	MuSiC	NNLS
mAD	0.029	0.031	0.066
RMSD	0.039	0.046	0.95
Pearson	0.99	0.98	0.93
Spearman	0.97	0.98	0.91

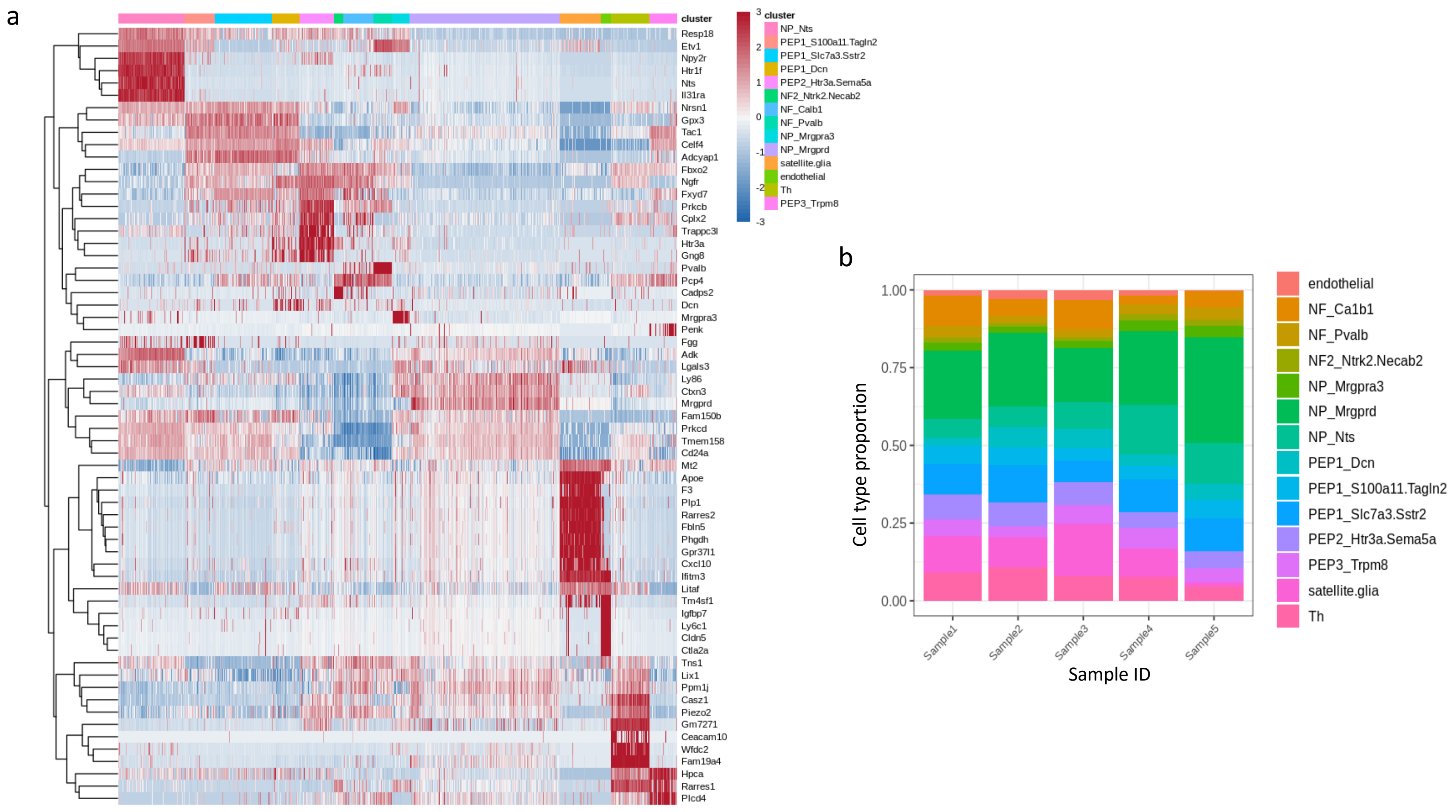
a
cluster
Resp18
Etv1
Npy2r
Htr1f
Nts
Il31ra
Nrsn1
Gpx3
Tac1
Celf4
Adcyap1
Fbxo2
Ngfr
Fxyd7
Prkcb
Cplx2
Trappc3l
Htr3a
Gng8
Pvalb
Pcp4
Cadps2
Dcn
Mrgpra3
Penk
Fgg
Adk
Lgals3
Ly86
Ctxn3
Mrgprd
Fam150b
Prkcd
Tmem158
Cd24a
Mt2
Apoe
F3
Plp1
Rarres2
Fbln5
Phgdh
Gpr37l1
Cxcl10
Ifitm3
Litaf
Tm4sf1
Igfbp7
Ly6c1
Cldn5
Ctla2a
Tns1
Lix1
Ppm1j
Casz1
Piezo2
Gm7271
Ceacam10
Wfdc2
Fam19a4
Hpca
Rarres1
Plcd4
3
2
1
0
-1
-2
-3
cluster
NP_Nts
PEP1_S100a11.Tagln2
PEP1_Slc7a3.Sstr2
PEP1_Dcn
PEP2_Htr3a.Sema5a
NF2_Ntrk2.Necab2
NF_Calb1
NF_Pvalb
NP_Mrgpra3
NP_Mrgprd
satellite.glia
endothelial
Th
PEP3_Trpm8
b
1.00
0.75
0.50
0.25
0.00
Cell type proportion
Sample1
Sample2
Sample3
Sample4
Sample5
Sample ID
endothelial
NF_Calb1
NF_Pvalb
NF2_Ntrk2.Necab2
NP_Mrgpra3
NP_Mrgprd
NP_Nts
PEP1_Dcn
PEP1_S100a11.Tagln2
PEP1_Slc7a3.Sstr2
PEP2_Htr3a.Sema5a
PEP3_Trpm8
satellite.glia
Th

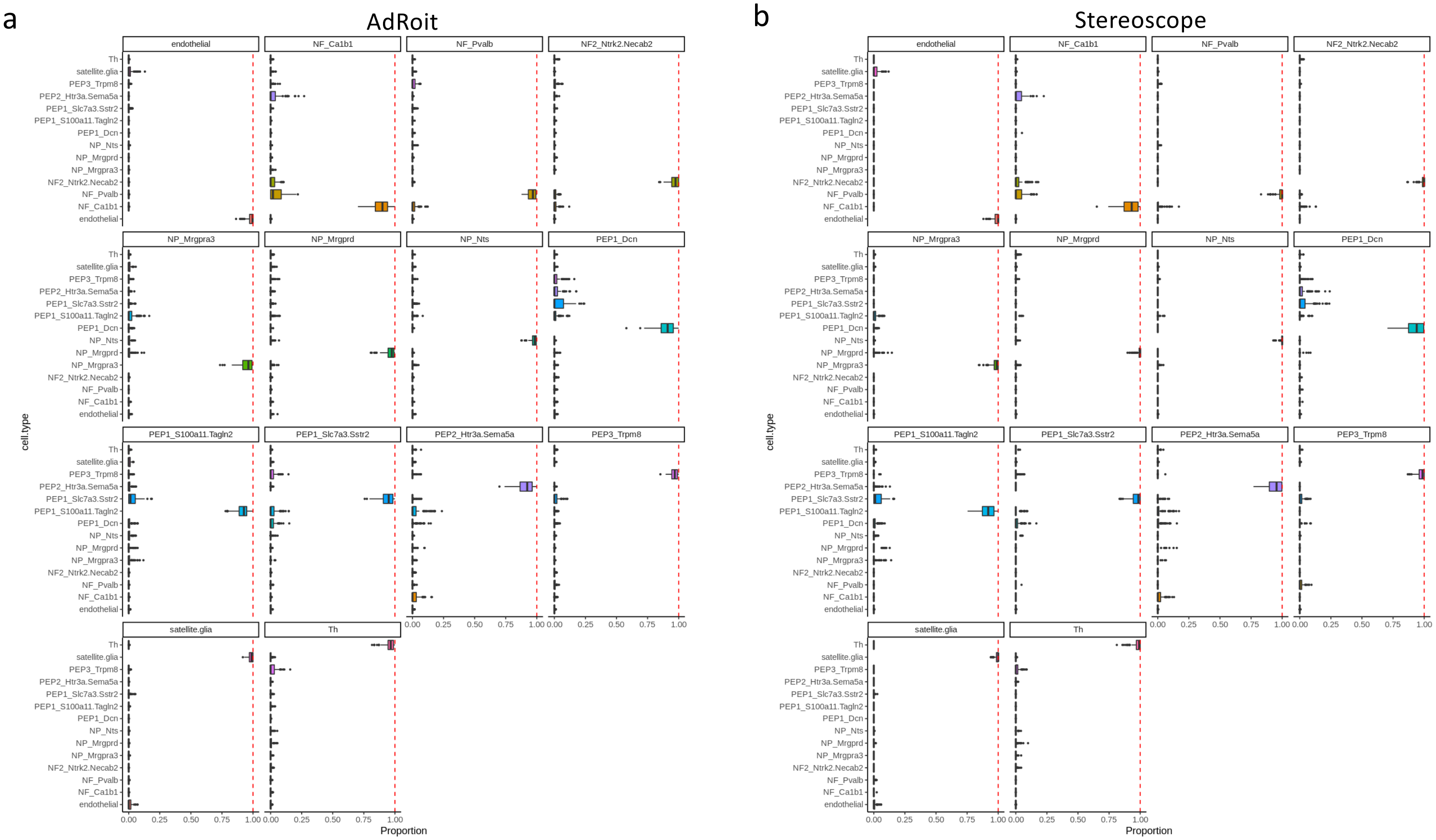
a
AdRoit
b
Stereoscope
endothelial
NF_Ca1b1
NF_Pvalb
NF2_Ntrk2.Necab2
NP_Mrgpra3
NP_Mrgprd
NP_Nts
PEP1_Dcn
PEP1_S100a11.Tagln2
PEP1_Slc7a3.Sstr2
PEP2_Htr3a.Sema5a
PEP3_Trpm8
satellite.glia
Th
cell.type
Th
satellite.glia
PEP3_Trpm8
PEP2_Htr3a.Sema5a
PEP1_Slc7a3.Sstr2
PEP1_S100a11.Tagln2
PEP1_Dcn
NP_Nts
NP_Mrgprd
NP_Mrgpra3
NF2_Ntrk2.Necab2
NF_Pvalb
NF_Ca1b1
endothelial
0.00
0.25
0.50
0.75
1.00
Proportion

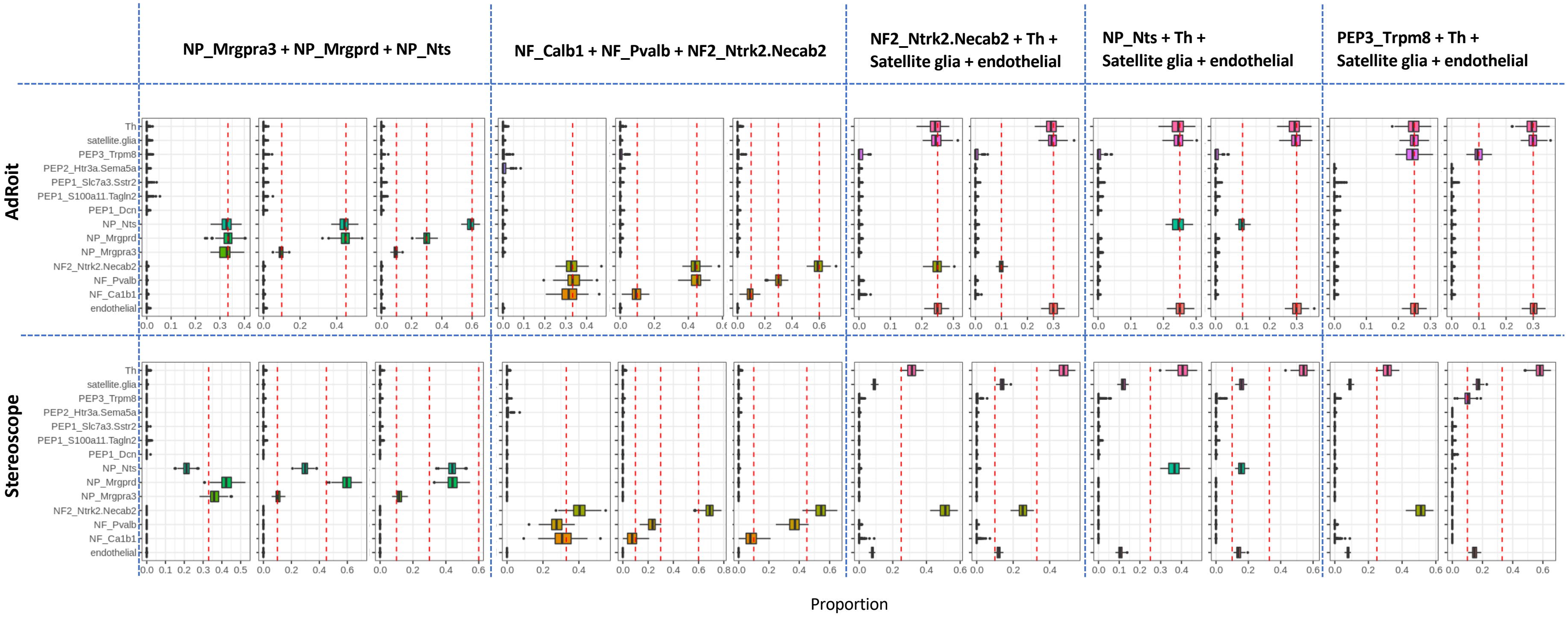
NP_Mrgpra3 + NP_Mrgprd + NP_Nts
NF_Calb1 + NF_Pvalb + NF2_Ntrk2.Necab2
NF2_Ntrk2.Necab2 + Th + Satellite glia + endothelial
NP_Nts + Th + Satellite glia + endothelial
PEP3_Trpm8 + Th + Satellite glia + endothelial
AdRoit
Stereoscope
Th
satellite.glia
PEP3_Trpm8
PEP2_Htr3a.Sema5a
PEP1_Slc7a3.Sstr2
PEP1_S100a11.Tagln2
PEP1_Dcn
NP_Nts
NP_Mrgprd
NP_Mrgpra3
NF2_Ntrk2.Necab2
NF_Pvalb
NF_Calb1
endothelial
0.0 0.1 0.2 0.3 0.4
0.0 0.2 0.4
0.0 0.2 0.4 0.6
0.0 0.1 0.2 0.3 0.4
0.0 0.2 0.4 0.6
0.0 0.2 0.4 0.6
0.0 0.1 0.2 0.3
0.0 0.1 0.2 0.3
0.0 0.1 0.2 0.3
0.0 0.1 0.2 0.3
0.0 0.1 0.2 0.3
0.0 0.1 0.2 0.3
0.0 0.1 0.2 0.3 0.4 0.5
0.0 0.2 0.4 0.6
0.0 0.2 0.4 0.6
0.0 0.2 0.4
0.0 0.2 0.4 0.6 0.8
0.0 0.2 0.4 0.6
0.0 0.2 0.4 0.6
0.0 0.2 0.4
0.0 0.1 0.2 0.3 0.4
0.0 0.2 0.4 0.6
0.0 0.2 0.4 0.6
0.0 0.2 0.4 0.6
Proportion

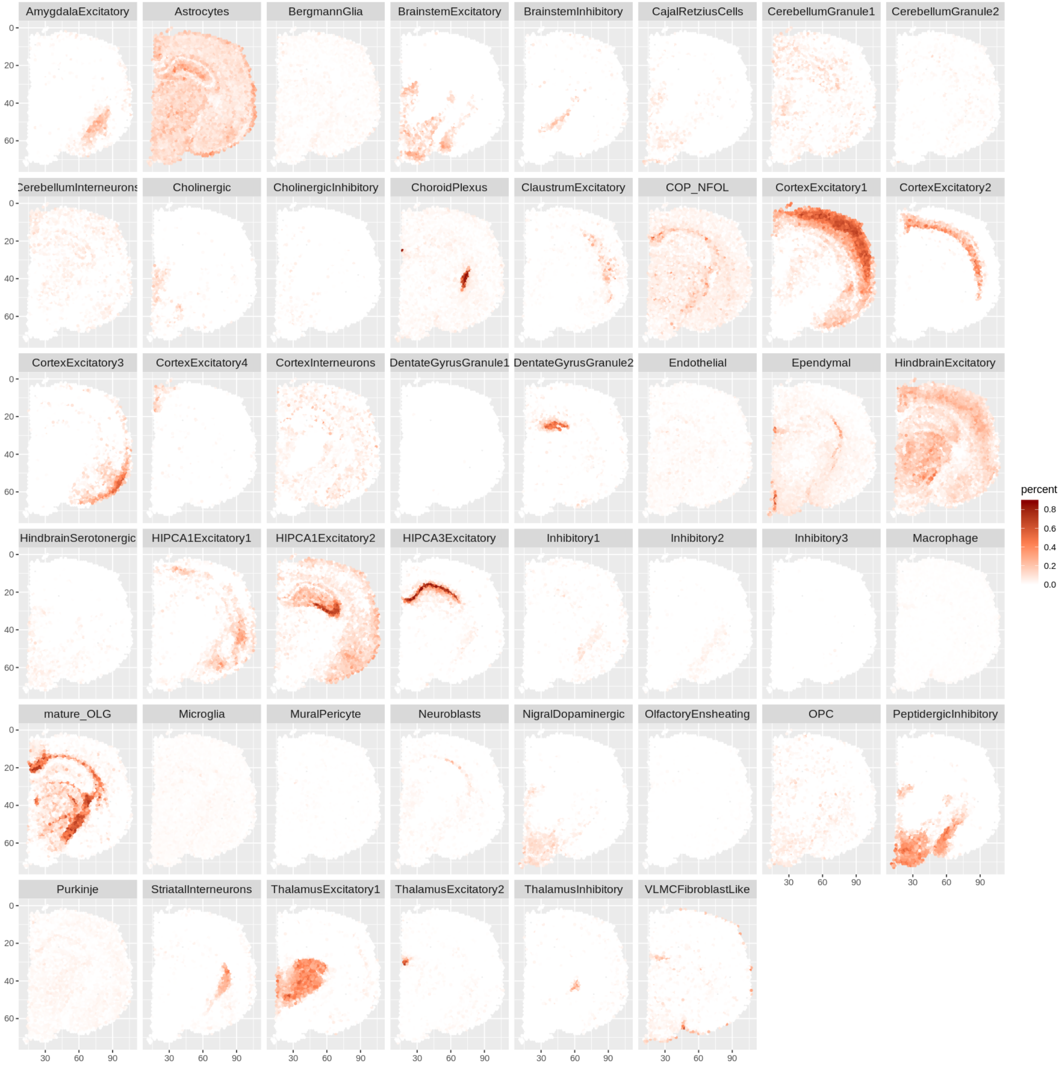
AmygdalaExcitatory
Astrocytes
BergmannGlia
BrainstemExcitatory
BrainstemInhibitory
CajalRetziusCells
CerebellumGranule1
CerebellumGranule2
CerebellumInterneurons
Cholinergic
CholinergicInhibitory
ChoroidPlexus
ClaustrumExcitatory
COP_NFOL
CortexExcitatory1
CortexExcitatory2
CortexExcitatory3
CortexExcitatory4
CortexInterneurons
DentateGyrusGranule1
DentateGyrusGranule2
Endothelial
Ependymal
HindbrainExcitatory
HindbrainSerotonergic
HIPCA1Excitatory1
HIPCA1Excitatory2
HIPCA3Excitatory
Inhibitory1
Inhibitory2
Inhibitory3
Macrophage
mature_OLG
Microglia
MuralPericyte
Neuroblasts
NigralDopaminergic
OlfactoryEnsheating
OPC
PeptidergicInhibitory
Purkinje
StriatalInterneurons
ThalamusExcitatory1
ThalamusExcitatory2
ThalamusInhibitory
VLMCFibroblastLike
0
20
40
60
30
60
90
percent
0.8
0.6
0.4
0.2
0.0

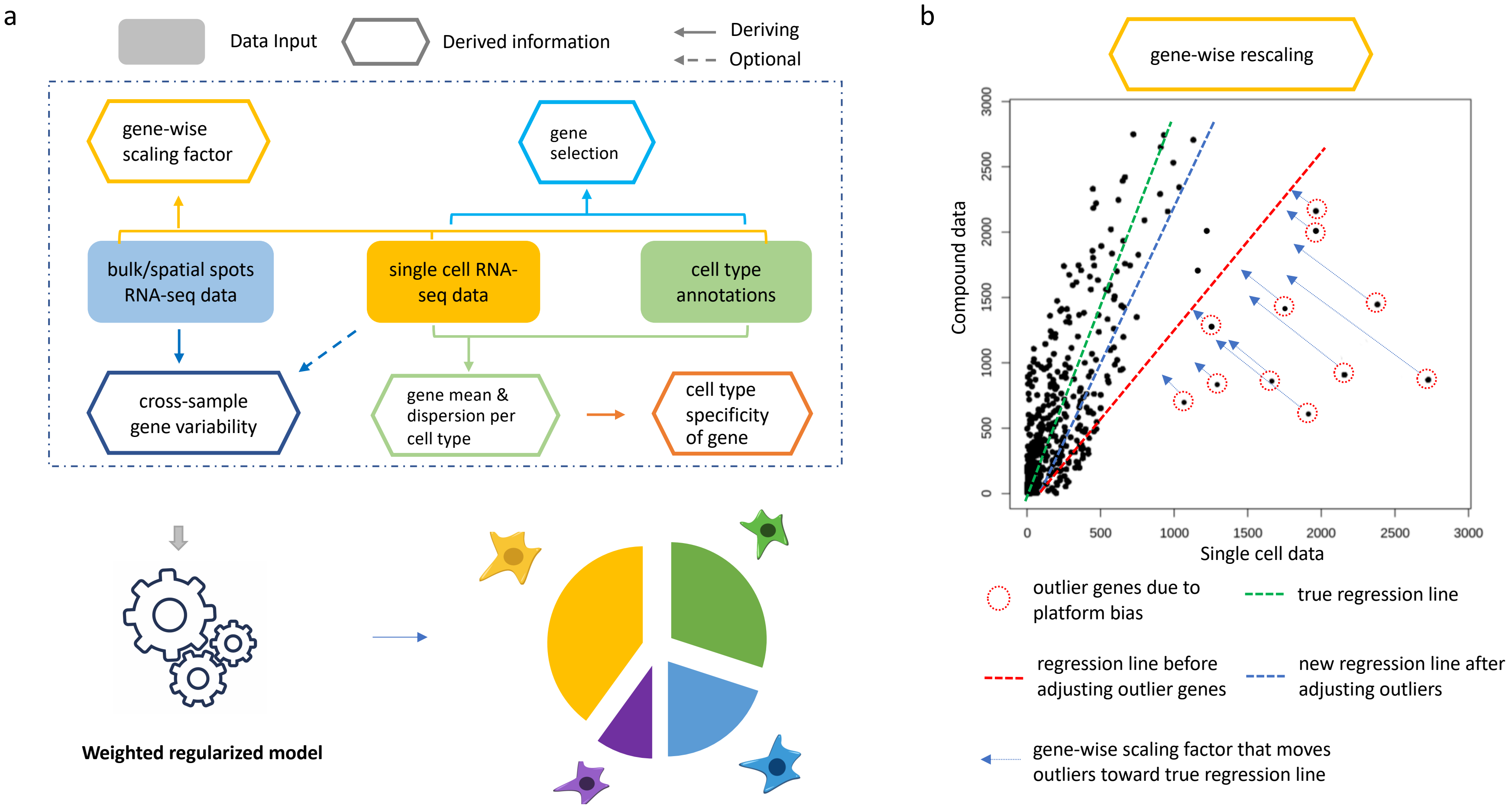
a
Data Input
Derived information
Deriving
Optional
gene-wise scaling factor
gene selection
bulk/spatial spots RNA-seq data
single cell RNA-seq data
cell type annotations
cross-sample gene variability
gene mean & dispersion per cell type
cell type specificity of gene
Weighted regularized model
b
gene-wise rescaling
Compound data
3000
2500
2000
1500
1000
500
0
0
500
1000
1500
2000
2500
3000
Single cell data
outlier genes due to platform bias
true regression line
regression line before adjusting outlier genes
new regression line after adjusting outliers
gene-wise scaling factor that moves outliers toward true regression line

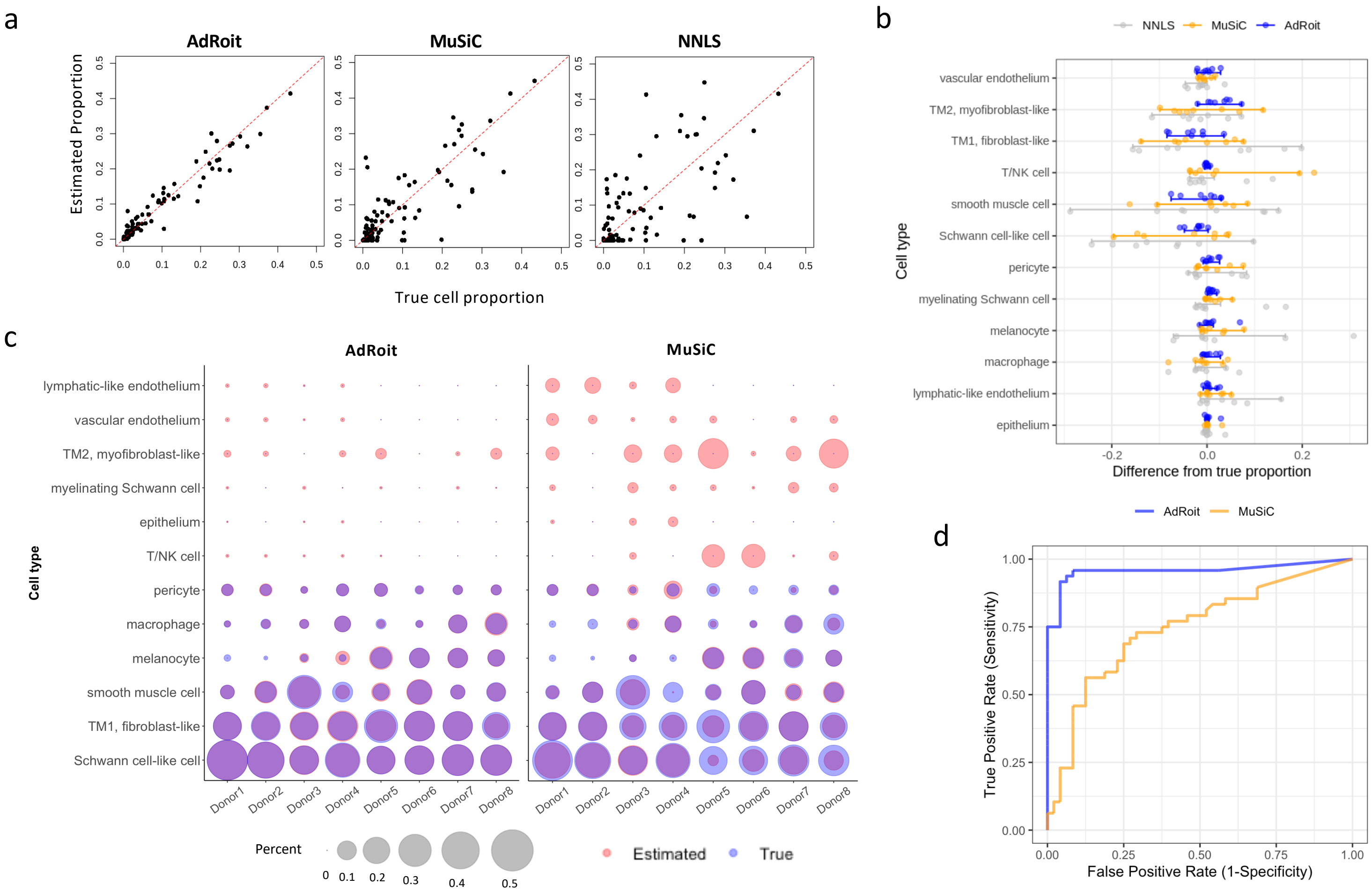

a
AdRoit
MuSiC
NNLS
Estimated Proportion
0.0
0.1
0.2
0.3
0.4
0.5
True cell proportion
b
NNLS
MuSiC
AdRoit
vascular endothelium
TM2, myofibroblast-like
TM1, fibroblast-like
T/NK cell
smooth muscle cell
Schwann cell-like cell
pericyte
myelinating Schwann cell
melanocyte
macrophage
lymphatic-like endothelium
epithelium
Cell type
-0.2
0.0
0.2
Difference from true proportion
c
AdRoit
MuSiC
lymphatic-like endothelium
vascular endothelium
TM2, myofibroblast-like
myelinating Schwann cell
epithelium
T/NK cell
pericyte
macrophage
melanocyte
smooth muscle cell
TM1, fibroblast-like
Schwann cell-like cell
Cell type
Donor1
Donor2
Donor3
Donor4
Donor5
Donor6
Donor7
Donor8
Percent
0
0.1
0.2
0.3
0.4
0.5
Estimated
True
d
AdRoit
MuSiC
1.00
0.75
0.50
0.25
0.00
True Positive Rate (Sensitivity)
0.00
0.25
0.50
0.75
1.00
False Positive Rate (1-Specificity)

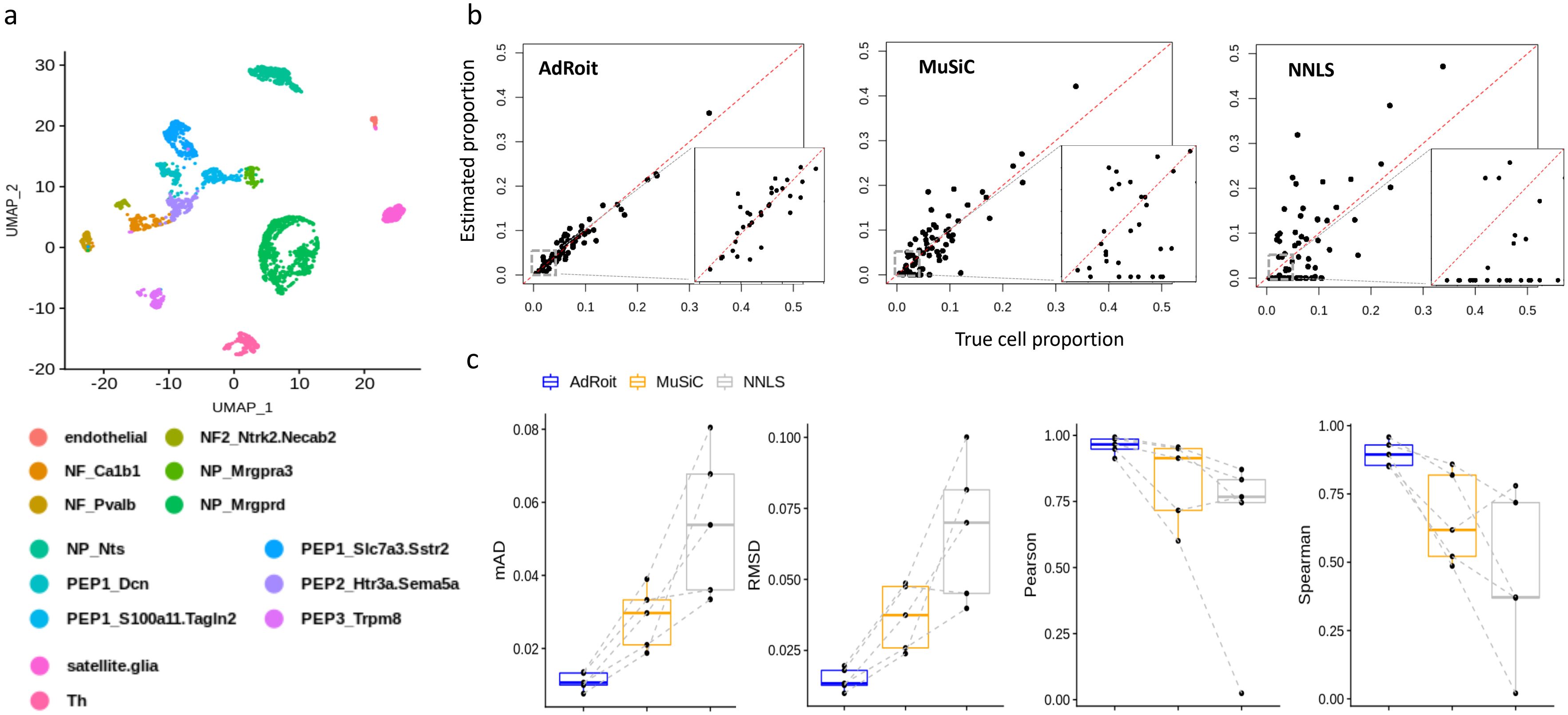
a
b
c
30
20
10
0
-10
-20
-20
-10
0
10
20
UMAP_1
UMAP_2
endothelial
NF_Ca1b1
NF_Pvalb
NF2_Ntrk2.Necab2
NP_Mrgpra3
NP_Mrgprd
NP_Nts
PEP1_Dcn
PEP1_S100a11.Tagln2
PEP1_Slc7a3.Sstr2
PEP2_Htr3a.Sema5a
PEP3_Trpm8
satellite.glia
Th
Estimated proportion
AdRoit
MuSiC
NNLS
0.0
0.1
0.2
0.3
0.4
0.5
True cell proportion
AdRoit
MuSiC
NNLS
mAD
0.02
0.04
0.06
0.08
RMSD
0.025
0.050
0.075
0.100
Pearson
0.00
0.25
0.50
0.75
1.00
Spearman
0.00
0.25
0.50
0.75
1.00

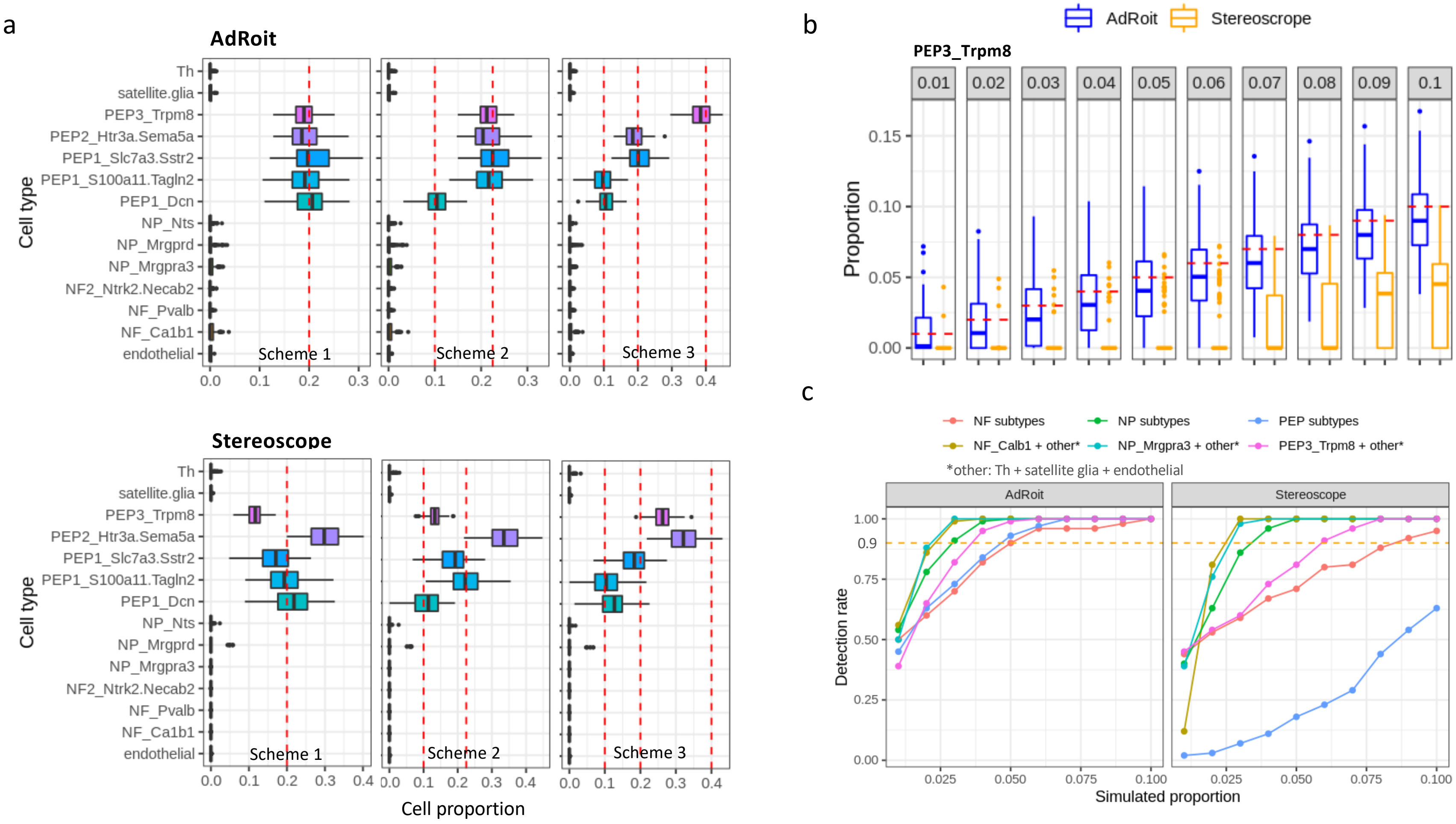
a
AdRoit
Th
satellite.glia
PEP3_Trpm8
PEP2_Htr3a.Sema5a
PEP1_Slc7a3.Sstr2
PEP1_S100a11.Tagln2
PEP1_Dcn
NP_Nts
NP_Mrgprd
NP_Mrgpra3
NF2_Ntrk2.Necab2
NF_Pvalb
NF_Ca1b1
endothelial
Cell type
Scheme 1
Scheme 2
Scheme 3
0.0 0.1 0.2 0.3
0.0 0.1 0.2 0.3
0.0 0.1 0.2 0.3 0.4
Stereoscope
Scheme 1
Scheme 2
Scheme 3
0.0 0.1 0.2 0.3 0.4
Cell proportion
b
AdRoit
Stereoscope
PEP3_Trpm8
0.01 0.02 0.03 0.04 0.05 0.06 0.07 0.08 0.09 0.1
Proportion
0.00 0.05 0.10 0.15
c
NF subtypes
NP subtypes
PEP subtypes
NF_Calb1 + other*
NP_Mrgpra3 + other*
PEP3_Trpm8 + other*
*other: Th + satellite glia + endothelial
AdRoit
Stereoscope
Detection rate
0.00 0.25 0.50 0.75 0.9 1.00
0.025 0.050 0.075 0.100
Simulated proportion

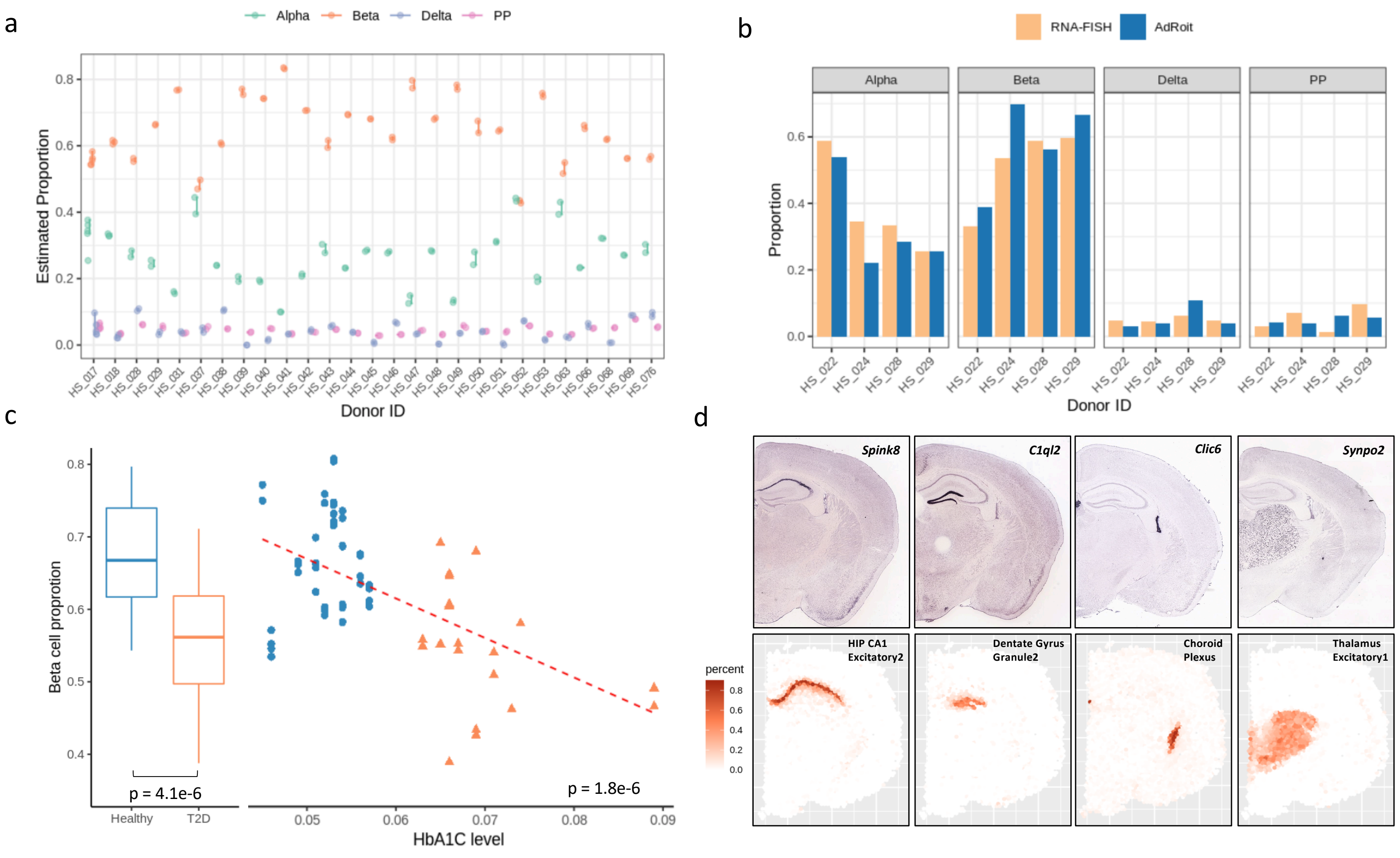
a
Alpha
Beta
Delta
PP
Estimated Proportion
0.8
0.6
0.4
0.2
0.0
HS_017
HS_018
HS_028
HS_029
HS_031
HS_037
HS_038
HS_039
HS_040
HS_041
HS_042
HS_043
HS_044
HS_045
HS_046
HS_047
HS_048
HS_049
HS_050
HS_051
HS_052
HS_053
HS_063
HS_066
HS_068
HS_069
HS_076
Donor ID
b
RNA-FISH
AdRoit
Alpha
Beta
Delta
PP
Proportion
0.6
0.4
0.2
0.0
HS_022
HS_024
HS_028
HS_029
Donor ID
c
Beta cell proprotion
0.8
0.7
0.6
0.5
0.4
p = 4.1e-6
Healthy
T2D
p = 1.8e-6
0.05
0.06
0.07
0.08
0.09
HbA1C level
d
Spink8
C1ql2
Clic6
Synpo2
percent
0.8
0.6
0.4
0.2
0.0
HIP CA1
Excitatory2
Dentate Gyrus
Granule2
Choroid
Plexus
Thalamus
Excitatory1